LÖNS, J. & SCHULZ, H. (1967). *Acta Cryst.* **23**, 434–436.
NYMAN, H. & HYDE, B. G. (1981). *Acta Cryst.* A**37**, 11–17.
ROGERS, D. (1981). *Acta Cryst.* A**37**, 734–741.
SETTER, N. & DEPMEIER, W. (1984). *Ferroelectrics*, **56**, 45–48.
SHELDRICK, G. M. (1978). *SHELXTL. An Integrated System for Solving, Refining and Displaying Crystal Structures from Diffraction Data.* Univ. of Göttingen, Federal Republic of Germany.

Acta Cryst. (1988). B**44**, 207–227

The Structure of {111} Age-Hardening Precipitates in Al–Cu–Mg–Ag Alloys

BY K. M. KNOWLES AND W. M. STOBBS

University of Cambridge, Department of Materials Science and Metallurgy, Pembroke Street, Cambridge CB2 3QZ, England

(*Received* 28 *July* 1987; *accepted* 9 *December* 1987)

Abstract

High-resolution transmission electron microscopy (HREM) of {111} precipitates in an Al–Cu–Mg–Ag alloy has been used to confirm by direct observation down ⟨110⟩ and ⟨211⟩ Al matrix zone axes that the structure of these precipitates in peak- and over-aged material is consistent with the monoclinic structure proposed by Auld [*Acta Cryst.* (1972), A**28**, S98] of $a = b = 4{\cdot}96$, $c = 8{\cdot}48$ Å, $\gamma = 120°$, rather than the hexagonal structure with $a = 4{\cdot}96$, $c = 7{\cdot}01$ Å proposed by Kerry & Scott [*Met. Sci.* (1984), **18**, 289–294]. Reexamination of the monoclinic structure suggested by Auld shows that the structure he proposes is in fact orthorhombic ($a = 4{\cdot}96$, $b = 8{\cdot}59$, $c = 8{\cdot}48$ Å), and is best regarded as a distortion of the structure of tetragonal θ-Al_2Cu precipitates found in over-aged Al–Cu alloys. A detailed reanalysis of electron diffraction patterns from this alloy in the light of HREM observations confirms that this structure and the relative thinness of these preciptates perpendicular to the {111} planes can indeed together satisfactorily account for the extra spots and streaks in the patterns.

1. Introduction

Suitable heat treatments of Al–Cu–Mg alloys with high Cu:Mg ratios and trace additions of silver can cause precipitates to nucleate and grow on {111} planes as well as {100} planes of the aluminium matrix (Taylor, Parker & Polmear, 1978; Chester & Polmear, 1983), and the occurrence of these thin disc-like precipitates significantly enhances the age-hardening characteristics of such alloys. The composition range within which these {111} precipitates have been found to occur suggests that they should be formed in the commercial Al–Cu–Mg–Ag alloys 201 and Avoir under suitable heat treatments, and indeed castings from such alloys are noted for their marked response to age hardening and for their good tensile properties (Iler, 1969; Taylor, Parker & Polmear, 1978). More recently, Brown Boveri have developed an experimental Al–Cu–Mg–Ag–Mn–Zr–Ti alloy for improved high-temperature strength and creep resistance, and the superior properties of this alloy over 2618 and 2219 arise from a fine dispersion of these {111} precipitates (Kubel, 1986; Polmear, 1986). It is therefore of interest to determine why it is energetically favourable for the {111} precipitates to form in these alloys and, from a knowledge of their structure and chemical composition, to determine whether such precipitates can be expected to occur in other aluminium alloy systems.

The role of the silver and the requirements of a high Cu:Mg ratio (Chester & Polmear, 1983) in promoting the {111} precipitation is as yet unclear. Taylor, Parker & Polmear (1978) suggested that the precipitates nucleate as Mg_3Ag, before growing and attaining an overall composition close to Al_2Cu. However, in agreement with the earlier work of Williams (1972), a recent study of precipitation processes in Al-rich Al–Mg–Ag alloys by Cousland & Tate (1986) has failed to isolate Mg_3Ag as a precipitating phase in ternary alloys, even in alloys with a high Mg to Ag ratio. Instead, Cousland & Tate showed that the phases that they observed containing only Ag and Mg atoms were of composition MgAg (their type 1 and type 2 GP zones). This would suggest that the nucleation mechanism for the {111} precipitates suggested by Taylor, Parker & Polmear (1978) is unlikely.

Furthermore, the structure of these precipitates is still a matter of debate. Auld (1972, 1986) has proposed a monoclinic unit cell on the basis of X-ray evidence with $a = b = 4{\cdot}96$, $c = 8{\cdot}48$ Å and $\gamma = 120°$, and showed that this structure can be considered to be a slightly distorted form of the structure of the incoherent θ-Al_2Cu precipitates (Guinier, 1942; Silcock, Heal & Hardy, 1953–1954; Laird & Aaronson, 1966). In contrast to this, Kerry & Scott (1984) have proposed a hexagonal unit cell with $a = 4{\cdot}96$ and $c = 7{\cdot}01$ Å from their analysis of electron diffraction patterns of peak-

0108-7681/88/030207-21$03.00 © 1988 International Union of Crystallography

aged samples, and were unable to index the patterns on the basis of Auld's unit cell. In response Auld (1986) has provided an example of how a reflection seen in the electron diffraction patterns could arise from the intersection with the Ewald sphere of a streak coming from precipitate reflections either just above or just below the Ewald sphere. Since the precipitates have been observed to be very thin along the [001] precipitate directions (20–30 Å), Auld's suggestion of the way to interpret the diffraction patterns clearly merits further examination.

For both of these proposed structures, the [001] direction in the precipitate is parallel to the corresponding ⟨111⟩ matrix direction defining the normal to the plane on which the precipitate occurs. The essential difference between the two proposed unit cells lies in the value of the 'c' parameter and its relation to the interplanar spacing of the {111} matrix planes. For the unit cell proposed by Auld, there is severe mismatch between the [001] precipitate and [111] matrix directions, while for Kerry & Scott's unit cell there is perfect matching between these two directions. Kerry & Scott account for the thinness of the precipitates along the ⟨111⟩ matrix directions by suggesting that the precipitates develop a series of intercellular stacking faults, arising from structural instabilities caused by the incorporation of copper into the precipitates, whereas the model proposed by Auld can account for the thinness in terms of the severe mismatch between the [001] precipitate and [111] matrix directions.

In this paper, we report the results of a detailed study using both high-resolution and dark-field transmission electron microscopy to clarify the nature of these precipitates. HREM in particular offers the opportunity of determining the precipitate structure by comparison of images with simulations for the two models from suitable low-index zones. In the light of our results, we also reexamine critically the interpretation of electron diffraction pattern data (Kerry & Scott, 1984) and show that they are indeed consistent with the unit cell suggested by Auld, although our reanalysis of his model shows that the conventional unit cell has orthorhombic rather than monoclinic symmetry. We also show in a companion paper (Knowles & Stobbs, 1988) that our electron diffraction pattern analysis can be applied to the interpretation of electron diffraction patterns from Al–Li–Cu alloys containing T_1 precipitates.

2. Structural models

Before presenting our experimental results, it is pertinent to discuss the two different models proposed for the {111} precipitates by Auld (1986) and Kerry & Scott (1984), and in particular to determine the atomic projections of the crystal structures down ⟨110⟩ and ⟨211⟩ Al matrix zone axes, since at least one precipitate variant will have its thin 'c' direction perpendicular to the projection direction in these cases.

Table 1. *Coordinates of atoms in Auld's* (1986) *monoclinic unit-cell description of the structure of* Ω *precipitates*

	x	y	z
Copper	$\frac{1}{2}$	0	$\frac{1}{4}$
	0	$\frac{1}{2}$	$\frac{3}{4}$
	$\frac{1}{2}$	0	$\frac{1}{4}$
	0	$\frac{1}{2}$	$\frac{1}{4}$
Aluminium	$\frac{1}{3}$	$\frac{1}{3}$	$\frac{1}{3}$
	$\frac{1}{2}$	$\frac{1}{2}$	$\frac{2}{3}$
	0	0	$\frac{1}{6}$
	0	0	$\frac{5}{6}$
	$\frac{1}{3}$	$\frac{2}{3}$	0
	$\frac{2}{3}$	$\frac{1}{3}$	0
	$\frac{1}{6}$	$\frac{5}{6}$	$\frac{1}{2}$
	$\frac{5}{6}$	$\frac{1}{6}$	$\frac{1}{2}$

2.1. *Auld's model*

Auld proposed a monoclinic unit cell for the {111} precipitates and assumed for his structure analysis that the main elements in the precipitates were aluminium and copper. The positions of the atoms in the unit cell that gave the best fit with the experimental X-ray data are shown in Table 1. Four unit cells seen in projection down [001] are shown in Fig. 1, from which it may be seen that there are mirror planes parallel to the (110) and (1$\bar{1}$0) planes of this unit cell, in addition to the mirror planes parallel to (001). Furthermore, there are diads not only along [001], but also along the [110] and

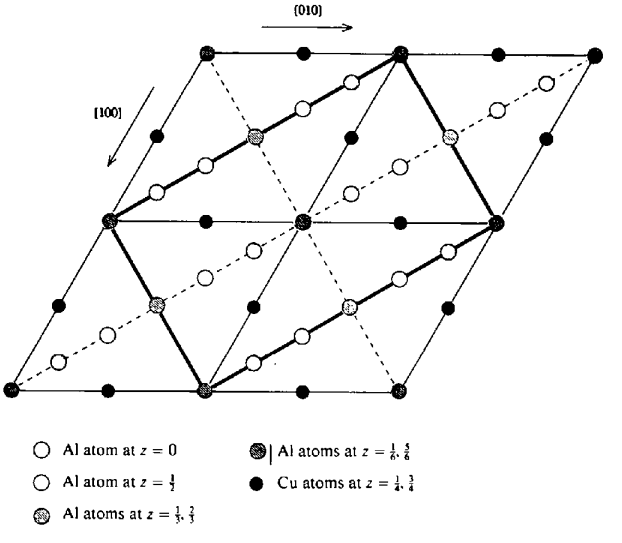

Fig. 1. Projection of four units cells down [001] for the monoclinic structure for the {111} Al–Cu–Mg–Ag precipitates proposed by Auld (1986), with the outline of the conventional orthorhombic unit cell indicated by thick continuous lines. Mirror planes parallel to the (1$\bar{1}$0), (110) and (001) planes are indicated by dashed lines. For clarity the diad axes along [1$\bar{1}$0], [110] and [001] have been omitted.

Table 2. *Coordinates of atoms in the conventional orthorhombic unit cell with* $a = 4{\cdot}96$, $b = 8{\cdot}59$ *and* $c = 8{\cdot}48$ Å *for the structure proposed by Auld* (1986)

Space group number 69. Space group *Fmmm*. Origin at *mmm*.

	Wyckoff notation	Symmetry	x	y	z	Occupancy
Al(1)	8(*h*)	*mm*	0	$\frac{1}{3}$	0	1·00
Al(2)	8(*i*)	*mm*	0	0	$\frac{1}{6}$	1·00
Cu	8(*f*)	222	$\frac{1}{4}$	$\frac{1}{4}$	$\frac{1}{4}$	1·00

$[1\bar{1}0]$ directions. It therefore follows that the conventional unit cell for his structure is not the monoclinic one proposed by Auld, but rather an orthorhombic one with $a = 4{\cdot}96$, $b = 4{\cdot}96\sqrt{3} = 8{\cdot}59$ and $c = 8{\cdot}48$ Å. The point-group symmetry of the structure is *mmm* and, since there are four lattice points per unit cell, the lattice type is orthorhombic *F*. The space-group symmetry is *Fmmm*, No. 69 in *International Tables for X-ray Crystallography* (1952). The atom positions of the Al and Cu atoms in this conventional unit cell are given in Table 2 using the Wyckoff notation and the description adopted in *Pearson's Handbook of Crystallographic Data for Intermetallic Phases* (Villars & Calvert, 1985). The monoclinic cell suggested by Auld has two lattice points (0,0,0) and $(\frac{1}{2},\frac{1}{2},\frac{1}{2})$ in a monoclinic *I* Bravais lattice, so that this description is not preferable on the grounds that it is based on a primitive unit cell for the structure.

Although the unit cell proposed by Auld has monoclinic symmetry, the lattice parameters conform to that of a hexagonal unit cell, and indeed Auld & Vietz (1969) used a hexagonal unit cell to index electron diffraction patterns in an earlier study of the structure of these precipitates. On this basis, the orientation relationship between the precipitates and matrix can be expressed as $[00.1]_\Omega \parallel [111]_{Al}$ and $[10.0]_\Omega \parallel [1\bar{1}0]_{Al}$, where the subscript Ω suggested by Chester & Polmear (1983) is used to designate the precipitate, rather than the symbol θ'_M suggested by Auld. Since there are four $\{111\}$ planes in Al and since on any particular plane the $[100]_\Omega$ direction in the monoclinic unit-cell description of the precipitate structure can be parallel to any one of the three $\langle 211\rangle$ directions, there are 12 distinct orientation relationships possible between precipitate and matrix. These orientation relationships are tabulated in Table 3 for both the monoclinic and orthorhombic unit cell descriptions of the precipitate structure. For a $[1\bar{1}0]$ beam direction in the matrix Al, there are six possible variants whose '*c*' directions are perpendicular to the electron beam, three variants on the (111) planes and three on the $(11\bar{1})$ planes. Within each group of three variants, two of the variants will be in symmetrically equivalent orientations and will therefore give HREM images which will be indistinguishable from one another. The third variant will have a different atomic projection and will therefore give HREM images which will be characteristically different from the two other variants. Thus, for a beam direction $[\bar{1}10]_{Al}$, the atomic projections of the precipitate variants Ω_{11} and Ω_{12} correspond to Fig. 2(*a*) and the atomic projection for Ω_{13} corresponds to Fig. 2(*b*). An analogous situation holds for atomic projections along $\langle 211\rangle_{Al}$ directions, and the two possible atomic projections of the precipitates in this orientation are shown in Fig. 3.

Table 3. Al–Cu–Mg–Ag Ω *precipitate orientation variants*

Variant designation	Al matrix directions parallel to the crystal axes for the monoclinic unit cell proposed by Auld (1986)			Al matrix directions parallel to the crystal axes for the conventional orthorhombic unit cell proposed in this paper		
	x_M	y_M	z_M	x_O	y_O	z_O
Ω_{11}	$[11\bar{2}]$	$[\bar{2}11]$	$[111]$	$[\bar{1}2\bar{1}]$	$[\bar{1}01]$	$[111]$
Ω_{12}	$[\bar{1}2\bar{1}]$	$[\bar{1}\bar{1}2]$	$[111]$	$[\bar{2}11]$	$[0\bar{1}1]$	$[111]$
Ω_{13}	$[\bar{2}11]$	$[1\bar{2}1]$	$[111]$	$[\bar{1}\bar{1}2]$	$[1\bar{1}0]$	$[111]$
Ω_{21}	$[1\bar{1}2]$	$[12\bar{1}]$	$[\bar{1}11]$	$[211]$	$[01\bar{1}]$	$[\bar{1}11]$
Ω_{22}	$[211]$	$[\bar{1}1\bar{2}]$	$[\bar{1}11]$	$[12\bar{1}]$	$[\bar{1}0\bar{1}]$	$[\bar{1}11]$
Ω_{23}	$[12\bar{1}]$	$[\bar{2}\bar{1}\bar{1}]$	$[\bar{1}11]$	$[\bar{1}1\bar{2}]$	$[\bar{1}\bar{1}0]$	$[\bar{1}11]$
Ω_{31}	$[\bar{1}12]$	$[\bar{1}\bar{2}\bar{1}]$	$[1\bar{1}1]$	$[\bar{2}\bar{1}1]$	$[0\bar{1}\bar{1}]$	$[1\bar{1}1]$
Ω_{32}	$[\bar{2}\bar{1}1]$	$[1\bar{1}\bar{2}]$	$[1\bar{1}1]$	$[\bar{1}2\bar{1}]$	$[10\bar{1}]$	$[1\bar{1}1]$
Ω_{33}	$[\bar{1}\bar{2}\bar{1}]$	$[21\bar{1}]$	$[1\bar{1}1]$	$[1\bar{1}\bar{2}]$	$[110]$	$[1\bar{1}1]$
Ω_{41}	$[112]$	$[1\bar{2}\bar{1}]$	$[11\bar{1}]$	$[2\bar{1}1]$	$[0\bar{1}\bar{1}]$	$[11\bar{1}]$
Ω_{42}	$[2\bar{1}1]$	$[\bar{1}\bar{1}\bar{2}]$	$[11\bar{1}]$	$[1\bar{2}\bar{1}]$	$[\bar{1}0\bar{1}]$	$[11\bar{1}]$
Ω_{43}	$[1\bar{2}\bar{1}]$	$[\bar{2}1\bar{1}]$	$[11\bar{1}]$	$[\bar{1}\bar{1}2]$	$[\bar{1}10]$	$[11\bar{1}]$

(1) Ω_{ij} denotes the *j*th variant on the *i*th set of $\{111\}_{Al}$ planes. The relationships between the crystal axes of the two unit cells are as follows:

$$x_O = x_M + y_M,\ y_O = y_M - x_M \text{ and } z_O = z_M$$

so that plane normal descriptions $\tilde{n}_O$ and $\tilde{n}_M$ are related through the formula

$$\tilde{n}_O = \tilde{n}_M \begin{bmatrix} 1 & \bar{1} & 0 \\ 1 & 1 & 0 \\ 0 & 0 & 1 \end{bmatrix}.$$

(2) When referred to the monoclinic unit cell, the relationships between the indexing of different precipitate variants within the four distinct groups precipitating out on each set of $\{111\}_{Al}$ planes are as follows:

$$\Omega_{i1}: (h, k, l)$$
$$\Omega_{i2}: (h+k, -h, l)$$
$$\Omega_{i3}: (k, -h-k, l)$$

for a given integer value of *i* between 1 and 4.

A particular feature of Auld's model of Ω precipitates is the close correspondence of the structure with that of θ-Al_2Cu precipitates. The orientation relationship between the orthorhombic unit cell for Ω and the tetragonal θ unit cell can be described as

$$[001]_\theta \parallel [100]_\Omega$$
$$[110]_\theta \parallel [010]_\Omega$$
$$[\bar{1}10]_\theta \parallel [001]_\Omega$$

with these vectors not only parallel to one another, but also corresponding to one another. Thus, the distortion

matrix S transforming the tetragonal θ structure into the orthorhombic Ω structure is

$$S = \begin{bmatrix} 1{\cdot}016 & 0{\cdot}0 & 0{\cdot}0 \\ 0{\cdot}0 & 1{\cdot}004 & 0{\cdot}0 \\ 0{\cdot}0 & 0{\cdot}0 & 0{\cdot}991 \end{bmatrix}$$

in a reference orthonormal axis system parallel to the Ω crystal axes, if one takes the 'a' and 'c' values for θ to be 6·05 and 4·55 Å respectively. Very little strain is therefore required to effect the formal tetragonal → orthorhombic structure change. This is most readily seen in the atomic projection of an Ω precipitate in Fig. 3(b), where the electron beam is parallel to a $\langle 211 \rangle_{Al}$ direction, and would be parallel to a fourfold axis direction in the precipitate if the lattice parameters b and c of the orthorhombic unit-cell description were equal.

It is therefore also relevant to compare the orientation relationship between Ω and Al with the orientation relationships between θ and Al. A number of different orientation relationships have been reported between θ and Al in both precipitation and lamellar eutectic systems (Guinier, 1942; Silcock, Heal & Hardy, 1953–1954; Laird & Aaronson, 1966; Vaughan & Silcock, 1967; Bonnet & Durand, 1973) and these have recently been classified by Bonnet (1980) on the basis of angle/axis disorientations. For the Ω/Al disorientation, we can approximate the Ω structure as θ and find the appropriate disorientation description for the orientation relationship

$$[110]_\theta \parallel [\bar{1}01]_{Al}$$
$$[\bar{1}10]_\theta \parallel [111]_{Al}$$
$$[001]_\theta \parallel [\bar{1}2\bar{1}]_{Al}$$

The result is a rotation of 35·26° about [110], so that $[110]_\theta \parallel [110]_{Al}$, $[1\bar{1}0]_\theta \parallel [1\bar{1}1]_{Al}$ and $[001]_\theta \parallel [\bar{1}12]_{Al}$. This angle/axis description is virtually identical to the angle/axis description given by Bonnet for a θ precipitate observed by Vaughan & Silcock (1967),

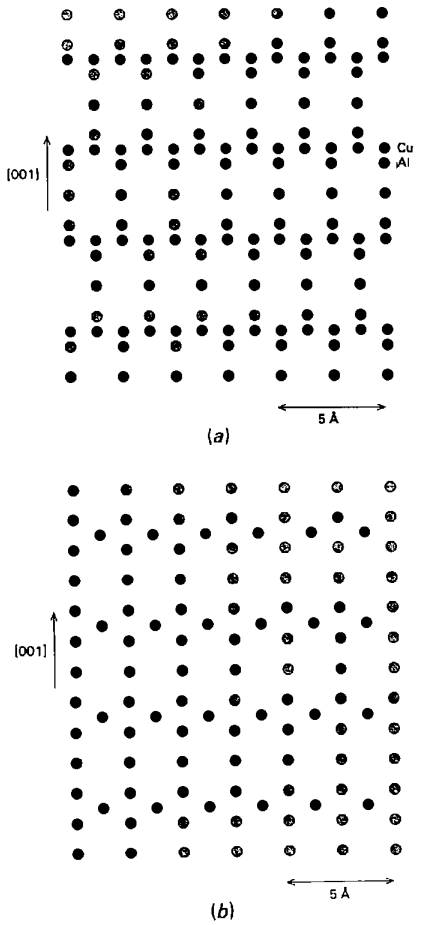

Fig. 2. (a) Atomic projection of the Ω_{11} and Ω_{12} precipitate variants down the $[\bar{1}10]_{Al}$ zone axis. (b) Atomic projection of the Ω_{13} precipitate variant down the same zone axis.

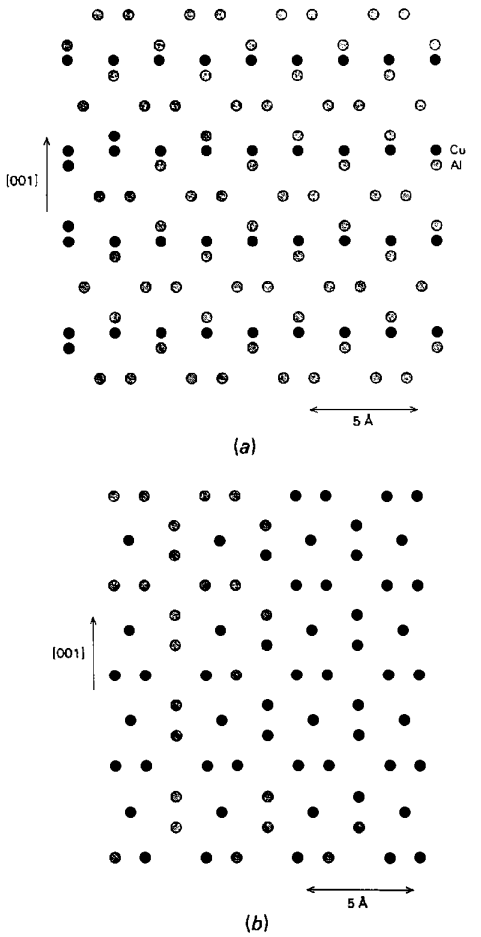

Fig. 3. (a) Atomic projection of the Ω_{11} and Ω_{13} precipitate variants down the $[\bar{2}11]_{Al}$ zone axis. (b) Atomic projection of the Ω_{12} precipitate variant down the same zone axis. Note how in (b) the projection would have fourfold symmetry at the positions of the Cu atoms if the dimensions 'b' and 'c' of the orthorhombic unit cell were equal.

designated by them a Vaughan II orientation. (The negative sign given by Bonnet for this angle/axis description merely gives a different symmetrically equivalent description to the one we have described). This indicates that the structure proposed by Auld is best regarded as a distortion of the structure of θ-Al_2Cu precipitates, and that the orientation relationship between the $\{111\}$ precipitates and the matrix Al can be understood as being one of the orientation relationships observed between θ and Al, albeit not one of the commonly reported orientation relationships.

2.2. *Kerry & Scott's model*

Kerry & Scott (1984) proposed a hexagonal unit cell for Ω with $a = 4{\cdot}96$ and $c = 7{\cdot}01$ Å, the latter dimension three times the $\{111\}$ interplanar spacing in Al. They based their structural model of the precipitates on close registry between the $(0001)_\theta$ planes and $(111)_{Al}$ planes and suggested that the hexagonal unit cell of the precipitate could simply be considered as a continuation of the ... *ABCA* ... stacking sequence of the (111) close-packed planes in Al, but with one in every three Al atom sites substituted by a Cu atom site to give an overall precipitate composition of Al_2Cu. They accounted for the streaking observed in electron diffraction patterns by suggesting that stacking fault sequences such as *ABC*|*BCA*|*CAB* developed in the precipitates because of the difficulty of incorporating Cu into the structure. This model therefore differs in two important aspects from the one proposed by Auld (1986). Firstly, the '*c*' dimension of the precipitate is different, and, secondly, there are only four possible orientation variants of the precipitate. Therefore, we would expect all high-resolution images of precipitates from, for example, the $\langle 110\rangle_{Al}$ zones to differ only if there are clear differences in the stacking sequences parallel to the [001] direction, and not because of any inherent difference in the atomic projection of the basic unit cell of the precipitate.

2.3. *Comparison with other precipitate structures*

Auld & Vietz (1969) noted that the lattice dimensions of Ω were similar to that of the T_1 phase in Al–Li–Cu. This latter phase was originally characterized by Hardy & Silcock (1955–1956) to be of an approximate composition Al_2CuLi with a hexagonal unit cell of $a = 4{\cdot}97$ and $c = 9{\cdot}34$ Å. The '*c*' dimension is therefore almost exactly four times the $\{111\}_{Al}$ interplanar spacing. T_1 has the same orientation relationship with Al as the hexagonal description of Ω and also precipitates as thin platelets on $\{111\}_{Al}$ planes, giving rise to streaking in electron diffraction patterns (Noble & Thompson, 1972; Huang & Ardell, 1986, 1987; Meyer & Dubost, 1986; Rioja & Ludwiczak, 1986; Cassada, Shiflet & Starke, 1987). The fine detail of the electron diffraction patterns from T_1-containing alloys is also similar to those of Ω-containing alloys [see, for example, the electron diffraction patterns of Huang & Ardell (1987)]. Interestingly, the interpretation of such electron diffraction patterns has also been a matter of debate. It has even been suggested by Rioja & Ludwiczak (1986) and Eikum & Narayanan (1986) that these diffraction patterns provide evidence for a precursor phase T'_1. However, other work by Huang & Ardell (1986, 1987) and Cassada, Shiflet & Starke (1987) has suggested that some of the detail in these diffraction patterns can arise from streaked reflections intersecting the Ewald sphere, an explanation similar to Auld's (1986) for the interpretation of electron diffraction patterns in Ω-containing alloys. As we show in a companion paper on

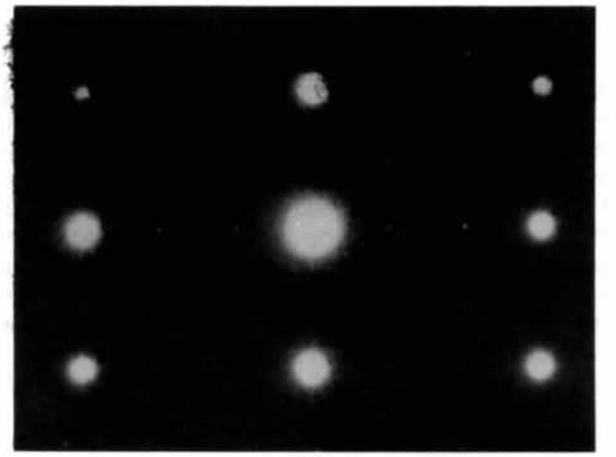

(*a*)

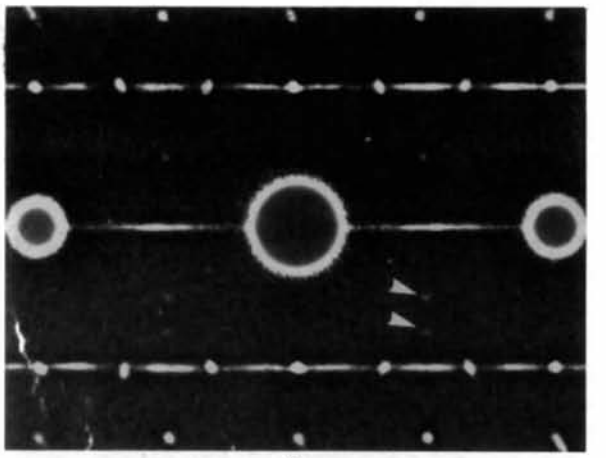

(*b*)

Fig. 4. (*a*) Electron diffraction pattern from a $\langle 211\rangle_{Al}$ zone taken with 500 kV electrons. (*b*) Detail of (*a*) around 000 showing the faint spots at $\frac{1}{2}$, $\frac{3}{2}$, $\frac{1}{2}$ and $\frac{1}{2}$, 1, 0 type positions (arrowed). This portion of the diffraction pattern has been digitized and the visibility of the faint reflections enhanced by a simple high-pass filter which has the subsidiary effect of weakening the intensity at the centre of the Al matrix diffraction spots.

T_1 precipitates (Knowles & Stobbs, 1988), the explanation by Huang & Ardell (1987) using a stereographic projection procedure is valid only for an Ewald sphere of infinite radius, and hence does not explain subtle splitting of 'spots' at high g, nor has it accounted satisfactorily for the spots at positions such as $\frac{1}{2}, \frac{3}{2}, -\frac{1}{2}$ in $\langle\bar{2}11\rangle_{Al}$ electron diffraction patterns.

In addition to this phase, a survey of other Al-based alloy phases in *Pearson's Handbook of Crystallographic Data for Intermetallic Phases* (Villars & Calvert, 1985) shows that there are a number of phases with the $MgZn_2$-type structure (for example $MgZn_2$ itself, AgAlMg, AlCuHf and phases in Al–Cu–Sc and Al–Cu–Ta) which would also appear to have structural similarities with Ω, if only through the magnitude of their lattice parameters, and again the precipitation of such phases in Al alloys may be worth reexamination.

3. Experimental procedure

An alloy of composition Al–4%Cu–0·3%Mg–0·4%Ag by weight [one of the compositions studied by Chester & Polmear (1983)] was prepared from high-purity material by chill casting followed by hot rolling into 1 mm thick sheets. The alloy was solution treated at 790 K in a salt bath, after which it was cold-water quenched and aged for 24 h in a salt bath kept at 440 K. This composition and heat treatment was chosen deliberately as it has been shown to be particularly effective at producing the {111} Ω precipitates with only minimal θ' precipitation (Chester & Polmear, 1983).

Specimens for transmission electron microscopy were obtained by standard electropolishing techniques and examined at 100 kV in a Philips EM300 for the dark-field and electron diffraction work and at 500 kV in the Cambridge University HREM for the high-resolution work. This latter microscope has a C_s of 2·7 mm, giving a contrast transfer function which extends without zeros to better than 2 Å at Scherzer defocus.

4. Experimental results

Fig. 4(*a*) is an electron diffraction pattern from $[\bar{2}11]_{Al}$ and is a good example of the complexity of the diffraction patterns observed in this alloy system. In addition to the spots indicated by Kerry & Scott in Fig. 4 of their paper in their schematic of this zone, faint spots are discernible at positions such as $\frac{1}{2}, \frac{5}{6}, \frac{1}{6}$ and $\frac{1}{2}$, 1, 0. These faint spots can be highlighted by digitizing the

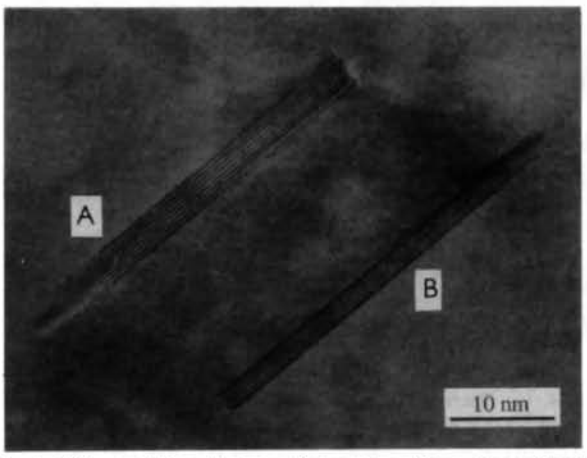

Fig. 5. High-resolution electron micrographs of two Ω precipitates labelled *A* and *B* on $(111)_{Al}$ with the electron beam parallel to $[\bar{2}11]_{Al}$. The HREM images from the two precipitates are distinctly different. $\Delta F \simeq -300$ Å.

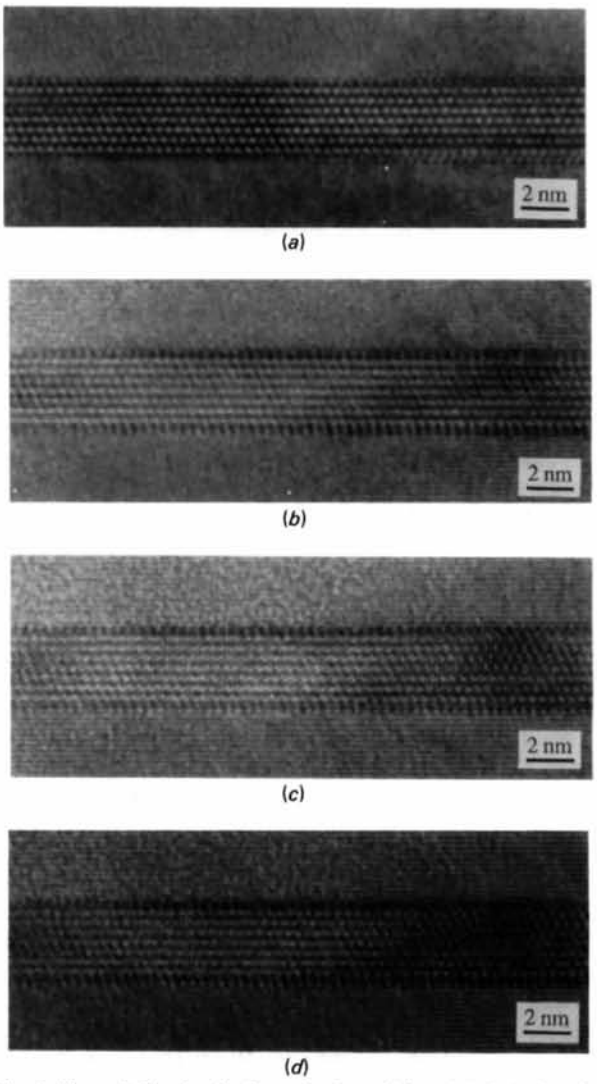

Fig. 6. Through-focal series from the Ω precipitate labelled *A* in Fig. 5. Approximate defocus values are (*a*) $\Delta F = -300$, (*b*) $\Delta F = -400$, (*c*) $\Delta F = -600$ and (*d*) $\Delta F = -800$ Å.

electron diffraction pattern and then filtering the pattern using a simple high-pass filter. The effect of this filter is to intensify those areas where the intensity changes rapidly and weaken those areas where the intensity remains constant (Fig. 4*b*).

In this orientation, the (111) matrix planes can be imaged, but other planar spacings such as $(02\bar{2})_{Al}$ are beyond the resolution of the microscope. A high-resolution image at this orientation is shown in Fig. 5, and it is clear that the two Ω precipitates marked *A* and *B* have distinctly different images. It is particularly striking that one of the precipitates has a square image and one a centred rectangular image, just as a simple weak-phase-object approximation would predict for the orthorhombic model of the precipitates (see also §6). Confirmation that these two precipitates do indeed have symmetrically different images comes from the through-focal series of these precipitates in Figs. 6 and 7. These images therefore rule out a hexagonal structure for the Ω precipitates. Direct measurements from the micrographs give an interplanar spacing of 4·2 (1) Å for the planes in the precipitate parallel to $(111)_{Al}$. This spacing readily correlates with half the '*c*' lattice parameter of the orthorhombic unit cell proposed here in §2.1 for the Ω precipitates. While detailed image simulations are needed to determine whether such measurements accurately represent the *true* interplanar spacings in the precipitates, because of their thinness, these images strongly support the orthorhombic structural model, and clearly negate the model proposed by Kerry & Scott (1984).

Other examples of high-resolution images from the Ω precipitates in this orientation are shown in Fig. 8. The images appeared to be very sensitive to small local specimen-dependent angular deviations away from $[\bar{2}11]_{Al}$, and Fig. 8(*c*) is a good example of this. The images emphasize the thinness of the Ω precipitates in the $[111]_{Al}$ direction and also demonstrate that the precipitate–matrix interfaces are planar, with very few interfacial steps. Furthermore, the tendency of the precipitates to adopt a hexagonal plate morphology of the precipitates can be confirmed directly – in a $\langle 211 \rangle_{Al}$ orientation the electron beam is along one of the vertices of a hexagon for both possible symmetrically distinct precipitate orientations, and the sharpness of

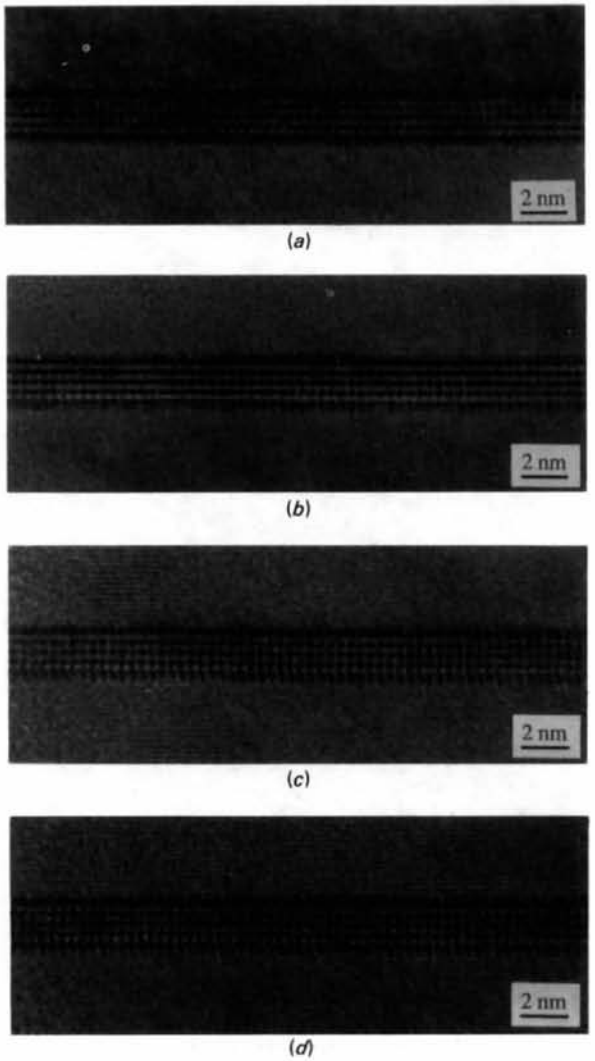

Fig. 7. Through-focal series from the Ω precipitate labelled *B* in Fig. 5. The approximate defocus values for (*a*)–(*d*) are the same as for Fig. 6(*a*)–(*d*).

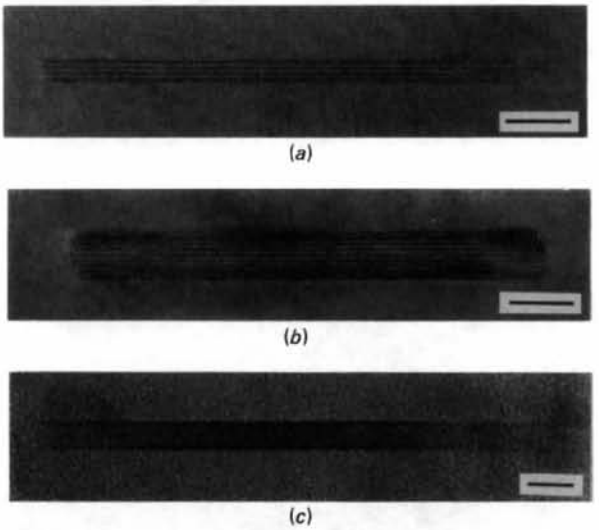

Fig. 8. Further HREM images from Ω precipitates with the electron beam parallel to $[\bar{2}11]_{Al}$. (*a*) A relatively thin precipitate. $\Delta F \simeq -800$ Å, (*b*) a relatively thick precipitate, $\Delta F \simeq -700$ Å and (*c*) an example of an HREM image where the specimen is bent and where the image changes sensitively as a function of position, giving an apparent randomness to the precipitate structure, because of the way in which different diffracted beams contribute to the image as a function of specimen tilt. $\Delta F \simeq 900$ Å. Scale markers correspond to 50 Å.

the interfaces perpendicular to the $(111)_{Al}$ planes demonstrates the hexagonal morphology.

Fig. 9 shows a diffraction pattern from $[1\bar{1}0]_{Al}$ at two different camera lengths to demonstrate the way in which high-order reflections in this orientation split into two or more spots, and to indicate the additional spots arising from both Ω and θ' precipitation. Streaking along 111_{Al} and $11\bar{1}_{Al}$ reciprocal-lattice directions arises from the Ω precipitation on these planes and the weaker streaking along 001_{Al} reciprocal-lattice directions from θ' precipitates. The streaking dies out at higher g values because of the finite curvature of the Ewald sphere. The splitting of spots at high g is of particular interest. As we shall show in §5, this splitting can be explained satisfactorily in terms of the intersection of streaked precipitate reflections with the Ewald sphere.

In this orientation the 111, $11\bar{1}$ and 002 matrix aluminium reflections all contribute to the image, giving a two-dimensional fringe pattern in the matrix. A through-focal series from one particular Ω precipitate in this zone orientation is shown in Fig. 10. The jagged nature of the 'end' of the precipitate in Fig. 10(*a*) is a consequence of both the hexagonal morphology of the precipitate and the electropolishing process, and is not necessarily indicative of any structural features. As for the $[\bar{2}11]_{Al}$ zone images, other symmetrically distinct images could also be obtained (Fig. 11) and again the interplanar spacing of the precipitate planes parallel to $\{111\}_{Al}$ were in agreement with the orthorhombic unit cell model for Ω.

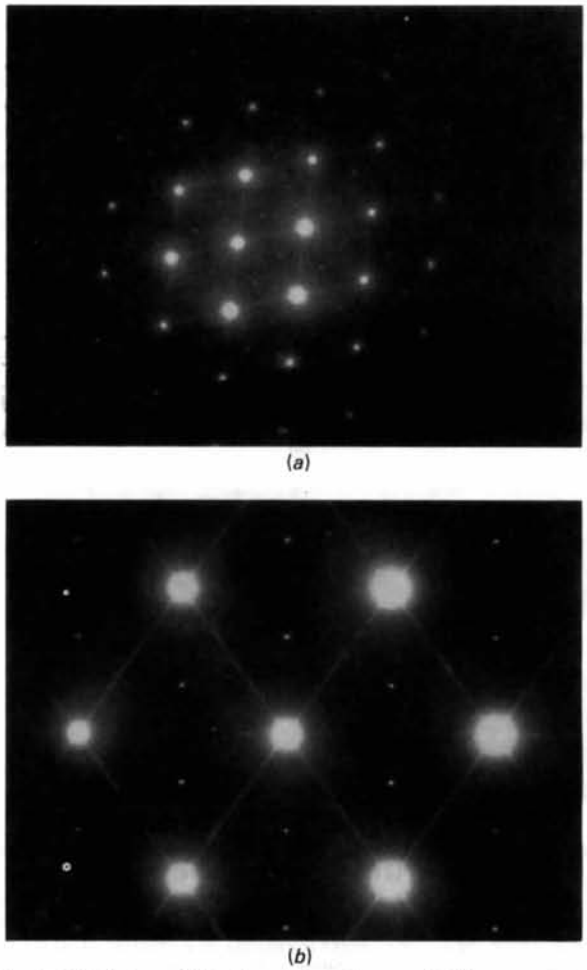

(*a*)

(*b*)

Fig. 9. (*a*) Electron diffraction pattern from a $\langle 110\rangle_{Al}$ zone, taken with 100 kV electrons, together with (*b*) detail of the diffraction pattern near 000.

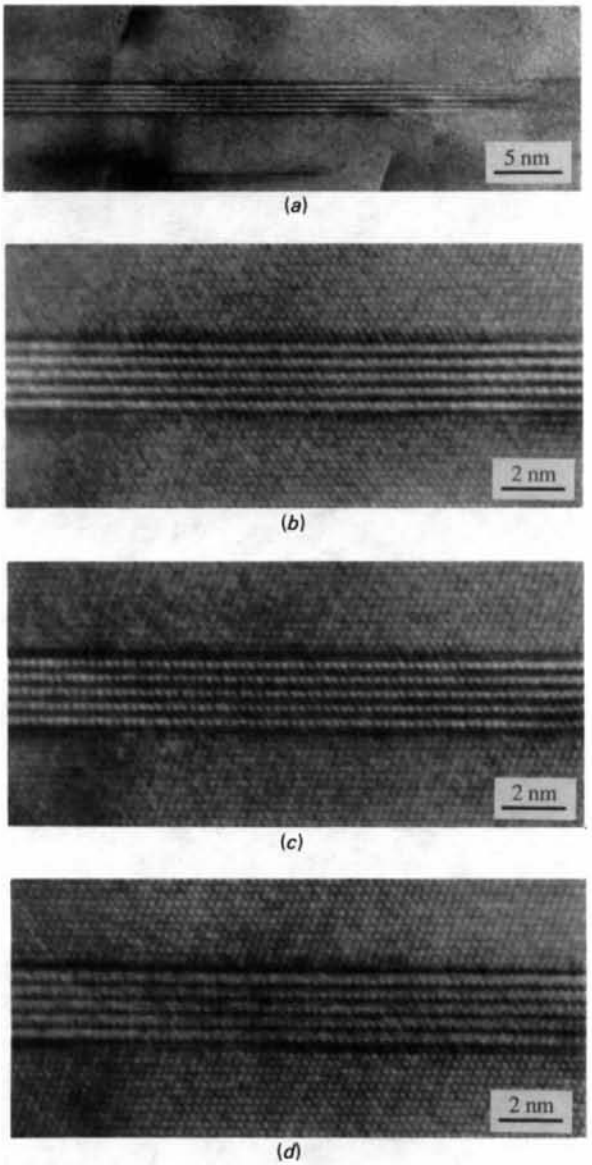

(*a*)

(*b*)

(*c*)

(*d*)

Fig. 10. HREM images of a precipitate on $(111)_{Al}$ with the electron beam parallel to $[\bar{1}10]_{Al}$. Approximate defocus values are (*a*) $\Delta F = -600$, (*b*) $\Delta F = -400$, (*c*) $\Delta F = -600$, and (*d*) $\Delta F = -800$ Å.

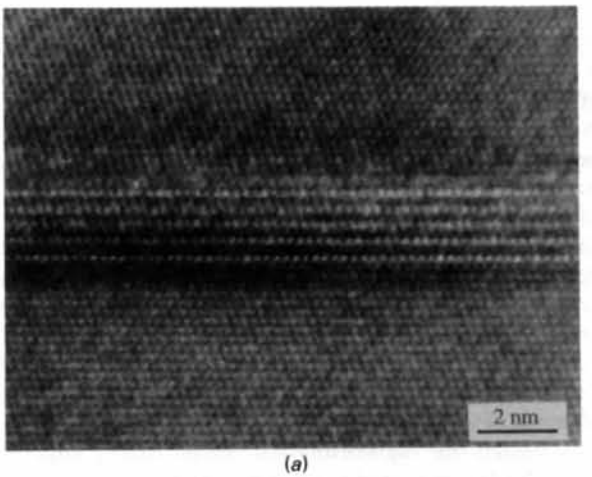

(*a*)

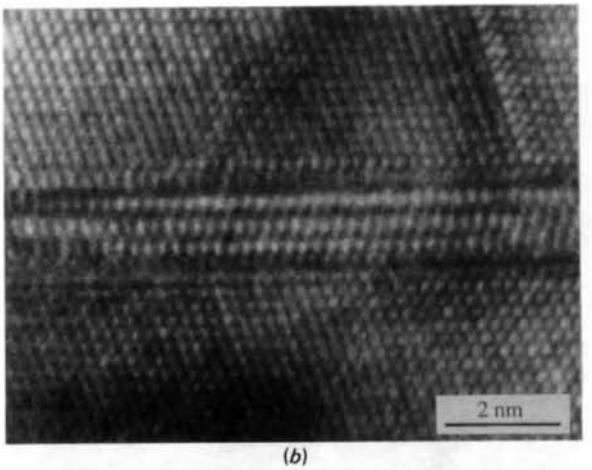

(*b*)

Fig. 11. Further HREM images from $[\bar{1}10]_{Al}$ showing images characteristically different from those in Fig. 10. In (*a*) $\Delta F \simeq -500$ and in (*b*) $\Delta F \simeq -800$ Å.

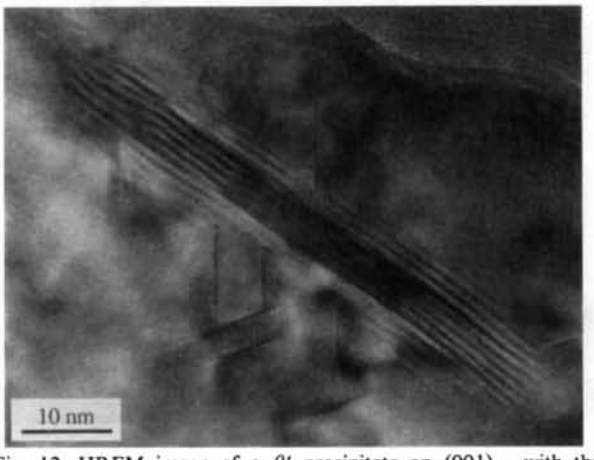

Fig. 12. HREM image of a θ' precipitate on $(001)_{Al}$, with the electron beam parallel to $[110]_{Al}$. The approximate defocus value is $\Delta F = -500$ Å. The features on $\{111\}_{Al}$ planes arise from radiation damage and are not Ω precipitates.

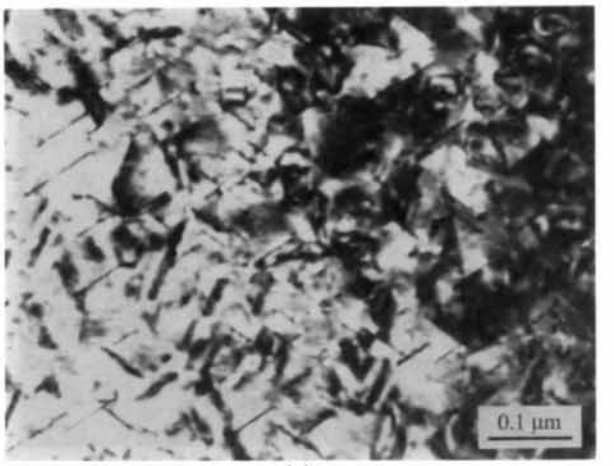

(*a*)

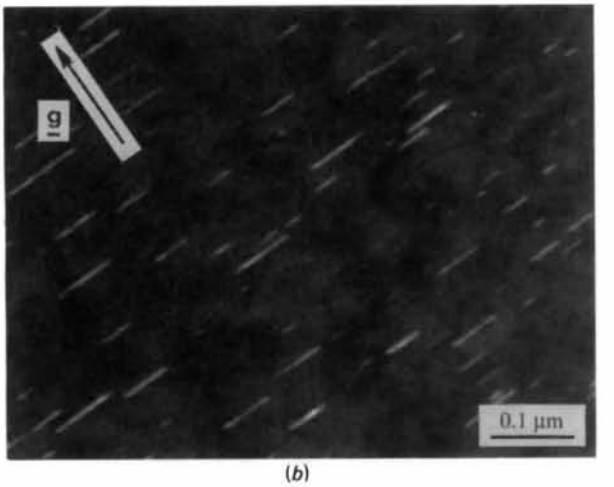

(*b*)

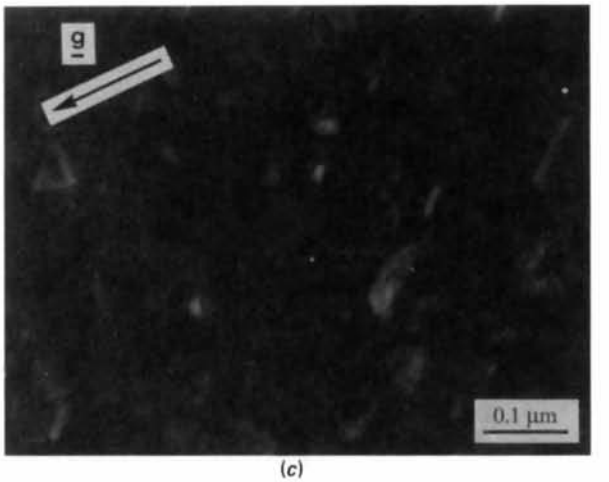

(*c*)

Fig. 13. (*a*) Bright-field image from a $\langle 1\bar{1}0\rangle_{Al}$ zone with Ω precipitation evident on the two $\{111\}_{Al}$ planes whose normals are perpendicular to the electron beam. (*b*), (*c*) Dark-field electron micrographs from a streaked Ω reflection and a 'spot' at $\frac{1}{3}$, $\frac{1}{3}$, 1 respectively. The area shown in both (*b*) and (*c*) is the same as in (*a*).

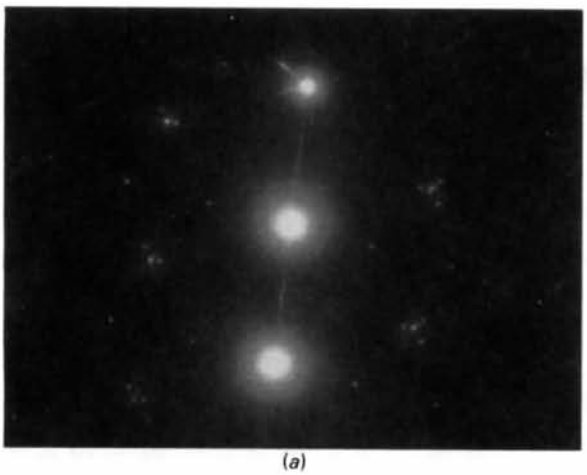

(a)

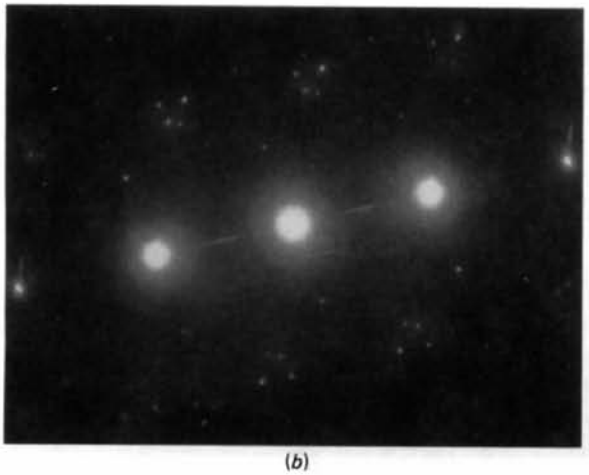

(b)

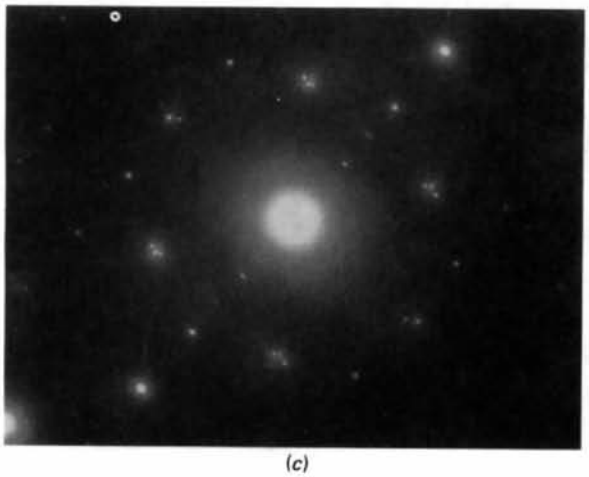

(c)

Fig. 14. Electron diffraction patterns obtained with 100 kV electrons by tilting the electron beam away from $[1\bar{1}0]_{Al}$: (*a*) $g = 11\bar{1}$ systematic maintained, with the beam direction some 7° from $[1\bar{1}0]$; (*b*) $g = 111$ systematic, with the beam direction some 9° from $[1\bar{1}0]$; (*c*) $g = 220$ systematic, with the beam direction some 7° from $[1\bar{1}0]$.

For comparison with the Ω precipitates, an HREM image from a θ' precipitate is shown in Fig. 12, taken in the $[1\bar{1}0]_{Al}$ zone axis orientation. This image is very different from those obtained from the Ω precipitates. In particular, the θ' precipitates are much broader than the Ω precipitates. There are also clear moiré fringes arising from the mismatch between 111_{Al} and $111_{\theta'}$ reflections, and these indicate that the θ' precipitates are ellipsoidal rather than hexagonal discs, as in the case of the Ω precipitates. The features on $\{111\}_{Al}$ planes in this micrograph arise from radiation damage (the threshold voltage for electron beam damage of aluminium is about 170 kV) and are not nuclei of the Ω precipitates, as they can be seen to grow under the influence of the electron beam.

Although our high-resolution results clearly support the orthorhombic model described in §2.1, this or any other viable structural model for the Ω precipitates

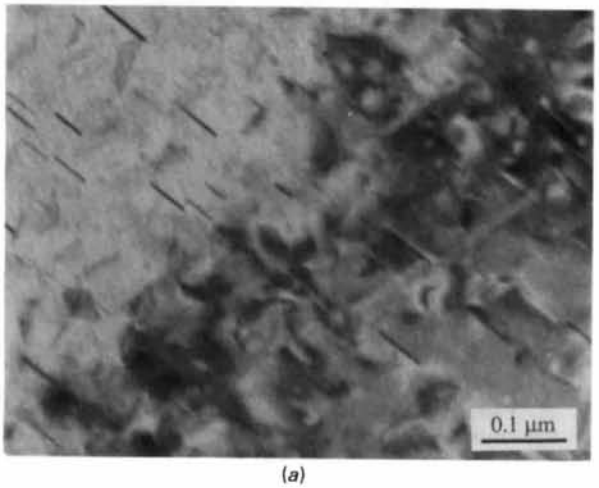

(a)

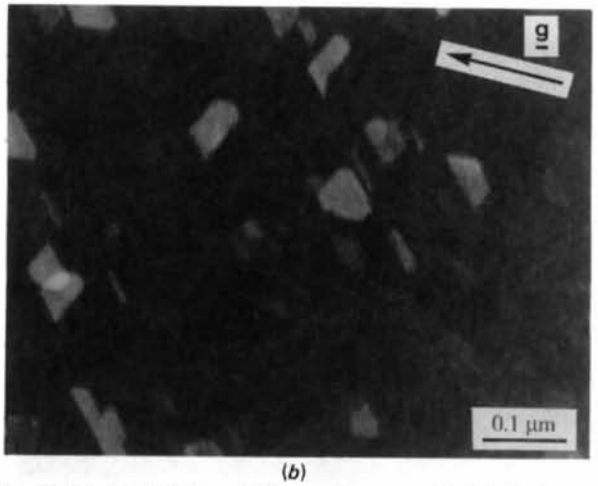

(b)

Fig. 15. (*a*) Bright-field and (*b*) complementary dark-field electron micrographs from a $\frac{1}{2}, \frac{3}{2}, -\frac{1}{2}$ spot in a $[\bar{2}11]_{Al}$ diffraction pattern. Only one set of $\{111\}_{Al}$ planes have Ω precipitates giving rise to the micrograph shown in (*b*).

must also be able to account for the complexity of the electron diffraction patterns from this alloy. For this reason, a series of dark-field and electron diffraction experiments was performed to determine which reflections in the diffraction patterns belonged to which variants, and to assess the effect of tilting on the position of reflections in the diffraction pattern. Dark-field images from reflections in the $[1\bar{1}0]_{Al}$ zone are shown in Fig. 13, from which it can be clearly seen that the spot at $\frac{1}{3}, \frac{1}{3}, 1$ arises from the precipitates on both the $(1\bar{1}1)$ and $(1\bar{1}\bar{1})$ aluminium planes, giving a ready explanation for the splitting of such reflections at high g in Fig. 9. Electron diffraction patterns obtained by tilting the electron beam away from $[1\bar{1}0]_{Al}$ are shown in Fig. 14, from which the tendency for the reflections to split into groups of two or more, as in Fig. 9, is readily apparent.

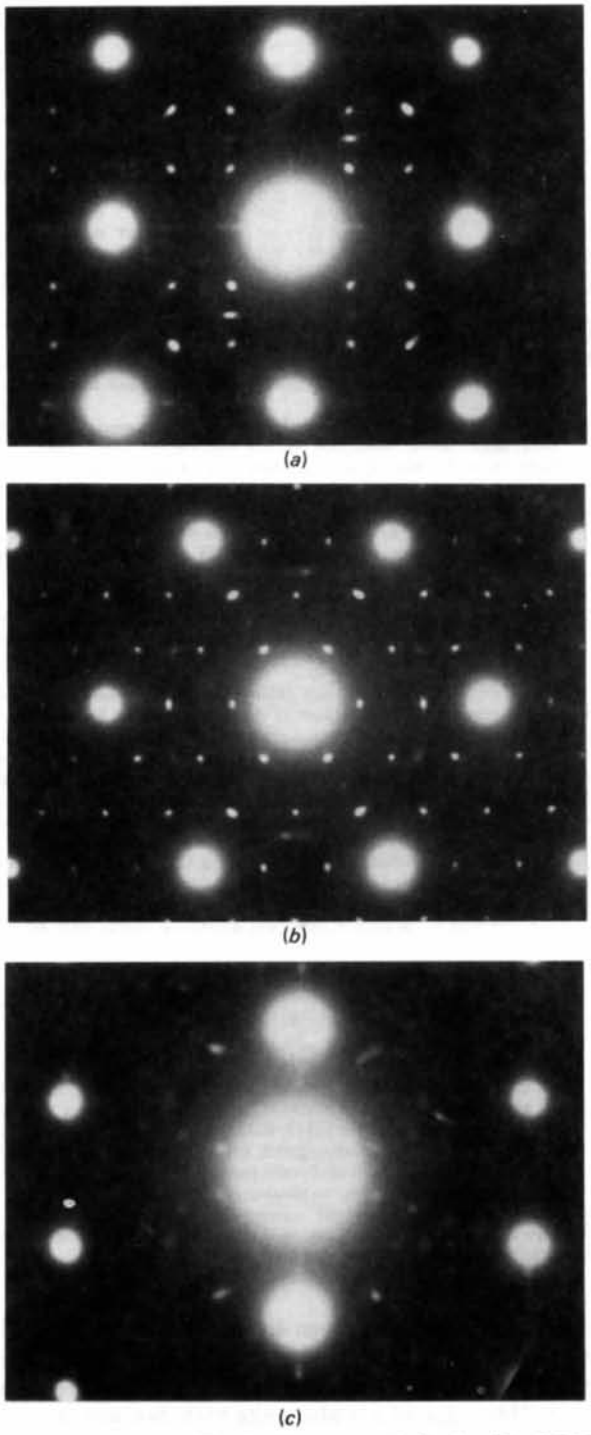

Fig. 16. Electron diffraction patterns obtained with 500 kV electrons from (*a*) a $\langle 001\rangle_{Al}$ zone axis, (*b*) a $\langle 111\rangle_{Al}$ zone axis and (*c*) a $\langle 310\rangle_{Al}$ zone axis.

Of particular interest are reflections at positions such as $\frac{1}{2}, \frac{3}{2}, -\frac{1}{2}$ seen in the electron diffraction diffraction pattern from $[\bar{2}11]_{Al}$. This reflection was not assigned indices by Kerry & Scott, and cannot be accounted for by their model, even on the basis of double diffraction. Complementary bright-field/dark-field images shown in Fig. 15 from this reflection show that it arises from the $(\bar{1}11)$ set of precipitates, set D of Fig. 4 of Kerry & Scott (1984). To complete our experimental data, electron diffraction patterns were also taken from $\langle 001\rangle_{Al}$, $\langle 111\rangle_{Al}$ and $\langle 310\rangle_{Al}$ zones (Fig. 16).

5. Electron diffraction pattern simulations

In order to account for the observed diffraction patterns, the details of the diffraction geometry pertinent to both the Ω and θ' sets of precipitates needs to be carefully examined, particularly in view of Kerry & Scott's analysis. As is well known [see, for example, Hirsch, Howie, Nicholson, Pashley & Whelan (1977)], the thinness of a feature parallel to a $[pqr]^*$ reciprocal-lattice direction produces a streak along $[pqr]^*$ inversely proportional to the thinness of the feature. Thus, as seen in Fig. 17, reflections with indices hkl which do not lie on the Ewald sphere may as a result of streaking intersect the Ewald sphere at a point B, thereby producing a spot or short streak in the diffraction pattern. Streaking of diffraction spots is of course particularly familiar in electron diffraction patterns, and formulae are readily available in the literature to account for the position of the spots, the lengths of the streaks and the displacement of a spot away from its 'true' position as a result of tilting away from a particular zone (Hirsch, Howie, Nicholson, Pashley & Whelan, 1977).

Using the equations discussed in the *Appendix*, a computer program was written to calculate where streaked reflections would occur for the experimental electron diffraction patterns in Figs. 4, 9, 14 and 16. Selected results of the calculations for the matrix Al zones $[1\bar{1}0]$, $[\bar{2}11]$ and $[001]$ are presented in Tables 4–8. The reflections listed in these tables are those from Ω only and satisfy the reflection conditions for the

Table 4. *Projected streak directions of {111} precipitates as a function of zone normal, referred to the cube axes of the matrix aluminium*

Zone $[uvw]$	Streak direction in reciprocal space $[pqr]^*$	Projected streak direction $[p'q'r']^*$	Angle between $[pqr]^*$ and $[p'q'r']^*$ (°)
$1\bar{1}0$	111	111	0·0
	$\bar{1}11$	001	54·74
	$1\bar{1}1$	001	54·74
	$11\bar{1}$	$11\bar{1}$	0·0
$\bar{2}11$	111	111	0·0
	$\bar{1}11$	111	70·53
	$1\bar{1}1$	$1\bar{2}4$	28·13
	$11\bar{1}$	$14\bar{2}$	28·13
001	111	110	35·26
	$\bar{1}11$	$\bar{1}10$	35·26
	$1\bar{1}1$	$1\bar{1}0$	35·26
	$11\bar{1}$	110	35·26

appropriate Bravais-lattice description. For example, in the orthorhombic F unit-cell description, all the precipitate reflections listed have hkl all odd or all even. However, it should be recognized that some of the reflections listed such as $hkl = 1\bar{1}0_M = 0\bar{2}0_O$, where the subscripts M and O denote monoclinic and orthorhombic unit-cell indexing respectively, will nevertheless have a zero structure factor if the structure and chemical composition of the Ω phase conforms to the atoms and atom positions given in Tables 1 and 2. A copy of the computer program and more comprehensive tabulations for both the Ω and θ' precipitate reflections can be obtained from the authors.

A more visually attractive but less accurate way of presenting the results of the computer program is to plot a schematic of the expected electron diffraction pattern. For these schematics, such as those in Fig. 18,† matrix Al spots were plotted as large circles if they lay within a distance parallel to the beam direction $[uvw]$ of less than 0·012 Å^{-1} from the Ewald sphere. Precipitate reflections hkl were plotted if ξ given by (2) had a modulus of less than 0·15 with $[pqr]^* = \langle 111 \rangle^*$ for the Ω precipitates or a modulus of less than 0·25 with $[pqr]^* = \langle 001 \rangle^*$ for the θ' precipitates. This value for ξ_{max} for the θ' precipitates is particularly high, but inspection of Fig. 9(*b*) shows that the streaking along 001 reciprocal-lattice directions, although faint in intensity because of the low population density of θ', is nevertheless appreciable in length. Moreover, it was found that having a ξ_{max} of less than 0·2 for the θ' precipitates could not explain the occurrence of the very faint $\frac{1}{2}$, 1, 0 type reflections on $\langle \bar{2}11 \rangle_{Al}$ diffraction patterns (*cf* Fig. 4*b*).

Precipitate reflections were also plotted if the deviation parameter s given by (3) had a modulus of less than 0·06 Å^{-1} for those cases where $[pqr]^*$ was almost or exactly perpendicular to the beam direction $[uvw]$. This value of s is also quite high, but was chosen to best reproduce the experimental electron diffraction patterns. Precipitate reflections were allocated streaks if the angle between $[pqr]^*$ and $[uvw]$ was greater than

† More extensive versions of Fig. 18 have been deposited with the British Library Document Supply Centre as Supplementary Publication No. SUP 44755 (9 pp.). Copies may be obtained through The Executive Secretary, International Union of Crystallography, 5 Abbey Square, Chester CH1 2HU, England.

Table 5. *Predicted positions of diffraction spots and streaks on a* $[1\bar{1}0]_{Al}$ *electron diffraction pattern for* 100 kV *electrons from an* Al *alloy with only* Ω *precipitates present, for comparison with the experimental* $\langle 110 \rangle_{Al}$ *electron diffraction pattern in Fig.* 9

PV	hkl_O	hkl_M	ξ_1	Q			ξ_2	B'		
Ω_{23}	$0\bar{2}0$	$1\bar{1}0$	0·0	0·667	0·667	0·0	0·003	0·667	0·667	−0·003
Ω_{33}	020	$\bar{1}10$	0·0	0·667	0·667	0·0	−0·003	0·667	0·667	0·003
Ω_{21}	220	020	0·0	1·333	1·333	0·0	0·011	1·333	1·333	−0·011
Ω_{31}	$\bar{2}\bar{2}0$	$0\bar{2}0$	0·0	1·333	1·333	0·0	−0·011	1·333	1·333	0·011
Ω_{21}	$1\bar{1}1$	101	−0·058	0·333	0·333	1·0	−0·054	0·333	0·333	0·996
Ω_{32}	$\bar{1}\bar{1}1$	$0\bar{1}1$	−0·058	0·333	0·333	1·0	−0·062	0·333	0·333	1·004
Ω_{22}	$1\bar{3}1$	$2\bar{1}1$	−0·058	1·0	1·0	1·0	−0·048	1·0	1·0	0·990
Ω_{31}	$\bar{1}\bar{3}1$	$1\bar{2}1$	−0·058	1·0	1·0	1·0	−0·067	1·0	1·0	1·010
Ω_{23}	$\bar{2}02$	$\bar{1}\bar{1}2$	−0·115	0·0	0·0	2·0	−0·102	0·0	0·0	1·987
Ω_{33}	$\bar{2}02$	$\bar{1}\bar{1}2$	−0·115	0·0	0·0	2·0	−0·128	0·0	0·0	2·013
Ω_{21}	$2\bar{2}2$	202	−0·115	0·667	0·667	2·0	−0·100	0·667	0·667	1·984
Ω_{31}	$\bar{2}\bar{2}2$	$0\bar{2}2$	−0·115	0·667	0·667	2·0	−0·131	0·667	0·667	2·016
Ω_{23}	$\bar{2}\bar{4}2$	$1\bar{3}2$	−0·115	1·333	1·333	2·0	−0·091	1·333	1·333	1·976
Ω_{33}	$\bar{2}42$	$\bar{3}12$	−0·115	1·333	1·333	2·0	−0·140	1·333	1·333	2·025

Nomenclature:

PV Precipitate variant (see Table 3).

hkl_O Reciprocal-lattice vector $\mathbf{r}^* = h\mathbf{a}^* + k\mathbf{b}^* + l\mathbf{c}^*$ of a precipitate reflection referred to the conventional orthorhombic unit cell described in Table 2.

hkl_M Reciprocal-lattice vector $\mathbf{r}^* = h\mathbf{a}^* + k\mathbf{b}^* + l\mathbf{c}^*$ of a precipitate reflection, referred to the monoclinic unit cell described by Auld (1986).

ξ_1 Magnitude of streak along $g_{\langle 111 \rangle}$ directions of the Al matrix for the streak to intersect an Ewald sphere of infinite radius, *i.e.* the plane normal to the zone axis $[1\bar{1}0]$. A negative number indicates that the centre of the streak, *i.e.* the position of hkl, is *inside* the Ewald sphere.

Q Point of intersection of streak with Ewald sphere of infinite radius (*cf.* Fig. 17).

ξ_2 As for ξ_1, but for an Ewald sphere appropriate for 100 kV electrons.

B' Point of intersection B of streak with the Ewald sphere for 100 kV electrons projected onto the plane perpendicular to the $[1\bar{1}0]$ zone normal (*cf.* Fig. 17).

(1) For the sake of brevity, this table gives only a selection of the calculated positions of the intersections of the streaks with the Ewald sphere, and only for one particular variant on a given set of {111} matrix planes. The indices hkl are allowed reflections for either the orthorhombic F Bravais lattice (h, k and l all odd or all even) or for the non-conventional monoclinic I Bravais lattice ($h + k + l$ even), as appropriate. hkl indices of other variants giving rise to a 'reflection' at a particular point in reciprocal space can be obtained using procedures such as those given in the footnotes to Table 3.

(2) The diffraction positions of variants Ω_{1j} and Ω_{4j} (j = 1 to 3) have not been tabulated, as they give rise to the streaking along $[111]^*$ and $[11\bar{1}]^*$ Al matrix reciprocal-lattice directions.

(3) The effective zones from which these diffraction effects arise are as follows:

$$\Omega_{21} \text{ and } \Omega_{31}: [1\bar{1}\bar{2}]_O = [10\bar{1}]_M$$
$$\Omega_{22} \text{ and } \Omega_{32}: [112]_O = [011]_M$$
$$\Omega_{23} \text{ and } \Omega_{33}: [101]_O = [111]_M$$

with respect to the conventional orthorhombic unit cell and the non-conventional monoclinic unit cell.

(4) All the positions at which the streaks intersect the plane normal to the zone axis are integer linear combinations of the two reciprocal-lattice vectors $\mathbf{a}_1^* = 0{\cdot}667, 0{\cdot}667, 0{\cdot}0$ and $\mathbf{a}_2^* = 0{\cdot}333, 0{\cdot}333, 1{\cdot}0$. For positions close to the origin, the indices are the appropriate linear combinations of the hkl indices corresponding to $\mathbf{a}_1^*$ and $\mathbf{a}_2^*$, for the particular variant. The values of B' (the positions one would expect to observe experimentally using a 100 kV transmission electron microscope) cannot be calculated so straightforwardly: rules such as those given in Table 6 for the non-conventional monoclinic I unit cell must be followed for these values.

Table 6. *Truth table for calculating the positions of other spots and streaks in Fig. 9, given the data in Table 5 for the monoclinic unit-cell description of the Ω precipitate structure*

Q_1	Q_1	Q_3	x_2	B_1'	B_1'	B_3'
Q_1	Q_1	$-Q_3$	$-x_{2c}$	B_{1c}'	B_{1c}'	$-B_{3c}'$
$-Q_1$	$-Q_1$	$-Q_3$	$-x_{2c}$	$-B_{1c}'$	$-B_{1c}'$	$-B_{3c}'$
$-Q_1$	$-Q_1$	Q_3	x_2	$-B_1'$	$-B_1'$	B_3'

In this table, the coefficients of Q, x_2 and B' are given for the four different distinct quadrants of the experimental diffraction pattern. The values in Table 5 were obtained for the quadrant for which all coefficients of Q were greater than or equal to zero. The subscript c denotes conjugate, *i.e.* for variant $2i$, take the value appropriate to the conjugate variant, variant $3i$ for i between 1 and 3.

Thus, for example, the diffraction spot at 1·333, 1·333, −2·0 on an Ewald sphere of infinite radius from variant 21 would be at 1·333, 1·333, −2·025 with an x_2 value of 0·140 for the Ewald sphere appropriate for 100 kV electrons.

Table 7. *Predicted positions of diffraction spots and streaks on a* $[\bar{2}11]_{Al}$ *electron diffraction pattern for* 500 kV *electrons from an alloy with only Ω precipitates present, for comparison with the experimental* $\langle 211\rangle_{Al}$ *electron diffraction pattern in Fig.* 4

PV	hkl_O	hkl_M	ξ_1		Q		ξ_2		B'	
Ω_{22}	$1\bar{3}1$	$2\bar{1}1$	−0·058	1·0	1·0	1·0	−0·061	1·001	1·001	1·001
Ω_{31}	$\bar{1}\bar{3}1$	$1\bar{2}1$	−0·058	1·0	1·0	1·0	−0·051	0·998	1·004	0·991
Ω_{41}	$1\bar{3}1$	$2\bar{1}1$	−0·058	1·0	1·0	1·0	−0·051	0·998	0·991	1·004
Ω_{21}	$\bar{1}1\bar{1}$	$\bar{1}0\bar{1}$	−0·109	−0·5	−0·167	−0·833	−0·110	−0·500	−0·166	−0·833
Ω_{21}	111	011	0·109	0·5	0·833	0·167	0·108	0·500	0·834	0·167
Ω_{22}	$2\bar{4}2$	$3\bar{1}2$	0·051	1·5	1·833	1·167	0·044	1·503	1·836	1·169
Ω_{31}	$02\bar{2}$	$\bar{1}1\bar{2}$	0·115	−0·667	0·0	−1·333	0·120	−0·668	0·003	−1·340
Ω_{41}	$\bar{1}1\bar{1}$	$\bar{1}01$	−0·058	−0·333	0·333	−1·0	−0·055	−0·334	0·330	−0·998
Ω_{21}	020	$\bar{1}10$	0·0	0·0	0·667	−0·667	−0·001	0·000	0·667	−0·666
Ω_{31}	$\bar{1}\bar{1}\bar{1}$	$0\bar{1}\bar{1}$	0·058	0·333	1·0	−0·333	0·060	0·332	1·002	−0·337
Ω_{41}	$0\bar{2}2$	$1\bar{1}2$	−0·115	0·667	1·333	0·0	−0·111	0·665	1·327	0·003
Ω_{31}	$\bar{2}40$	$1\bar{3}0$	0·0	1·333	2·0	0·667	0·013	1·329	2·009	0·649
Ω_{21}	$\bar{1}3\bar{1}$	$\bar{2}1\bar{1}$	−0·109	−0·5	0·5	−1·5	−0·112	−0·499	0·501	−1·499
Ω_{21}	131	$\bar{1}21$	0·109	0·5	1·5	−0·5	0·106	0·501	1·501	−0·499
Ω_{23}	$0\bar{6}2$	$3\bar{3}2$	0·051	1·5	2·5	0·5	0·042	1·503	2·503	0·503
Ω_{41}	$\bar{2}22$	$\bar{2}02$	−0·115	−0·667	0·667	−2·0	−0·105	−0·670	0·653	−1·993
Ω_{32}	$02\bar{4}$	$\bar{1}\bar{1}4$	−0·103	−0·333	1·0	−1·667	−0·094	−0·336	1·006	−1·678
Ω_{21}	040	$\bar{2}20$	0·0	0·0	1·333	−1·333	−0·004	0·001	1·335	−1·332
Ω_{43}	024	$\bar{1}14$	0·103	0·333	1·667	−1·0	0·111	0·331	1·656	−0·995
Ω_{31}	$\bar{2}\bar{2}\bar{2}$	$0\bar{2}\bar{2}$	0·115	0·667	2·0	−0·667	0·126	0·663	2·007	−0·681
Ω_{22}	$3\bar{1}1$	211	−0·058	1·0	2·333	−0·333	−0·065	1·002	2·336	−0·331
Ω_{21}	$\bar{1}5\bar{1}$	$\bar{3}2\bar{1}$	−0·109	−0·5	1·167	−2·167	−0·116	−0·498	1·169	−2·164
Ω_{21}	151	$\bar{2}31$	0·109	0·5	2·167	−1·167	0·102	0·502	2·169	−1·164
Ω_{22}	$4\bar{2}2$	312	0·051	1·5	3·167	−0·167	0·038	1·504	3·171	−0·162
Ω_{21}	060	$\bar{3}30$	0·0	0·0	2·0	−2·0	−0·009	0·003	2·003	−1·997
Ω_{32}	$\bar{1}3\bar{5}$	$\bar{2}1\bar{5}$	−0·045	0·0	2·0	−2·0	−0·028	−0·006	2·012	−2·023
Ω_{42}	$\bar{1}35$	$\bar{2}15$	0·045	0·0	2·0	−2·0	0·062	−0·006	1·977	−1·989
Ω_{33}	$06\bar{4}$	$\bar{3}3\bar{4}$	−0·103	1·0	3·0	−1·0	−0·079	0·992	3·016	−1·032
Ω_{42}	$\bar{2}06$	$\bar{1}\bar{1}6$	−0·012	1·0	3·0	−1·0	0·011	0·992	2·969	−0·985

(1) The definitions for the column headings are the same as in Table 5, except that ξ_2 is the magnitude of the streak when it intersects the Ewald sphere for 500 kV electrons, rather than for 100 kV electrons.

(2) For the sake of brevity, this table gives only a selection of the calculated positions of the intersections of the streaks with the Ewald sphere, and only for one particular variant on a given set of {111} matrix planes. *hkl* indices of other variants giving rise to a 'reflection' at a particular point in reciprocal space can be obtained using a procedure such as that given in the footnotes to Table 3.

(3) The diffraction positions of variants Ω_{1j} ($j = 1$ to 3) have not been tabulated here, as they give rise to the streaking along the [111]* Al matrix reciprocal-lattice directions.

(4) Unlike the case of the $[1\bar{1}0]$ and [001] zones, the *hkl* indexing of the diffraction spots and streaks arising from the Ω precipitates is not straightforward, as not all the 'reflections' from a particular Ω_{ij} variant arise from the same zone. In effect, some of the reflections arise from higher-order Laue zones.

Table 8. *Predicted positions of diffraction spots and streaks on a* $[001]_{Al}$ *diffraction pattern for* 500 kV *electrons for an* Al *alloy with only Ω precipitates present, for comparison with the experimental* $\langle 001\rangle_{Al}$ *electron diffraction pattern in Fig.* 16

PV	hkl_O	hkl_M	ξ_1		Q		ξ_2		B'	
Ω_{12}	$\bar{2}02$	$\bar{1}\bar{1}2$	−0·115	2·0	0·0	0·0	−0·122	2·007	0·007	0·0
Ω_{21}	$20\bar{2}$	$11\bar{2}$	0·115	2·0	0·0	0·0	0·108	1·993	0·007	0·0
Ω_{31}	$\bar{2}02$	$\bar{1}\bar{1}2$	−0·115	2·0	0·0	0·0	−0·122	2·007	−0·007	0·0
Ω_{41}	202	112	−0·115	2·0	0·0	0·0	−0·108	1·993	−0·007	0·0
Ω_{13}	$0\bar{2}0$	$1\bar{1}0$	0·0	−0·667	0·667	0·0	−0·002	−0·665	0·668	0·0
Ω_{43}	020	$\bar{1}10$	0·0	−0·667	0·667	0·0	0·002	−0·668	0·665	0·0
Ω_{23}	$0\bar{2}0$	$1\bar{1}0$	0·0	0·667	0·667	0·0	−0·002	0·665	0·668	0·0
Ω_{33}	020	$\bar{1}10$	0·0	0·667	0·667	0·0	−0·002	0·668	0·665	0·0
Ω_{11}	$0\bar{2}2$	$1\bar{1}2$	−0·115	1·333	0·667	0·0	−0·119	1·337	0·671	0·0
Ω_{42}	$0\bar{2}2$	$1\bar{1}2$	−0·115	1·333	0·667	0·0	−0·111	1·329	0·663	0·0
Ω_{21}	022	$\bar{1}12$	−0·115	−0·667	1·333	0·0	−0·119	−0·671	1·337	0·0
Ω_{31}	$0\bar{2}\bar{2}$	$1\bar{1}\bar{2}$	0·115	−0·667	1·333	0·0	0·111	−0·663	1·329	0·0
Ω_{12}	$0\bar{2}2$	$1\bar{1}2$	−0·115	0·667	1·333	0·0	−0·119	0·671	1·337	0·0
Ω_{41}	$0\bar{2}2$	$1\bar{1}2$	−0·115	0·667	1·333	0·0	−0·111	0·663	1·329	0·0
Ω_{21}	220	$02\bar{0}$	0·0	1·333	1·333	0·0	−0·006	1·327	1·340	0·0
Ω_{31}	$\bar{2}\bar{2}0$	$0\bar{2}0$	0·0	1·333	1·333	0·0	−0·006	1·340	1·327	0·0
Ω_{11}	202	112	−0·115	0·0	2·0	0·0	−0·122	0·007	2·007	0·0
Ω_{22}	202	112	−0·115	0·0	2·0	0·0	−0·122	−0·007	2·007	0·0
Ω_{32}	$\bar{2}0\bar{2}$	$\bar{1}\bar{1}\bar{2}$	0·115	0·0	2·0	0·0	0·108	0·007	1·993	0·0
Ω_{42}	$\bar{2}02$	$\bar{1}\bar{1}2$	−0·115	0·0	2·0	0·0	−0·108	−0·007	1·993	0·0
Ω_{11}	$1\bar{3}5$	$2\bar{1}5$	0·045	2·0	2·0	0·0	0·031	2·014	2·014	0·0
Ω_{23}	$06\bar{0}$	$3\bar{3}0$	0·0	2·0	2·0	0·0	−0·014	1·986	2·014	0·0
Ω_{33}	$06\bar{0}$	$\bar{3}30$	0·0	2·0	2·0	0·0	−0·014	2·014	1·986	0·0
Ω_{41}	$1\bar{3}5$	$2\bar{1}5$	0·045	2·0	2·0	0·0	0·059	1·986	1·986	0·0

(1) The definitions for the column headings are the same as in Table 7.

(2) For the sake of brevity, this table gives only a selection of the calculated positions of the intersections of the streaks with the Ewald sphere, and only for one particular variant on a given set of {111} matrix planes. *hkl* indices of other variants giving rise to a 'reflection' at a particular point in reciprocal space can be obtained using a procedure such as that given in Table 3.

45°, with the lengths of the streaks proportional to the projected length of $[pqr]^*$ onto the plane normal to $[uvw]$. If the angle between $[pqr]^*$ and $[uvw]$ was less than 72°, a circle was plotted at the position B' as

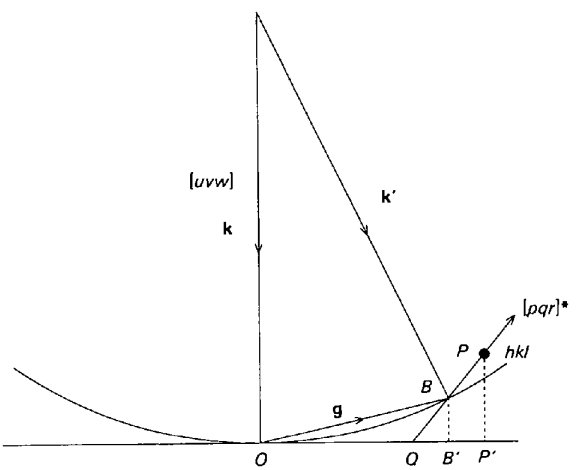

Fig. 17. The geometry of streaking in electron diffraction patterns. The electron beam is along $[uvw]$ and the direction of streaking of a diffraction spot P with indices *hkl* is along the reciprocal-lattice vector pqr^*, cutting the Ewald sphere at B and the plane perpendicular to the electron beam at Q. B' is the projection of B onto the plane normal to $[uvw]$.

indicated in Fig. 17, with the radius of the circle scaled to indicate the proximity of the precipitate reflection *hkl* to the Ewald sphere. θ' reflections are distinguished from Ω reflections in Fig. 18 by asterisks. Ω and θ' reflections for which the angles between $[pqr]^*$ and $[uvw]$ were greater than 72° had the centres of the streak denoted by small circles and asterisks respectively. The allocation of streaks and/or spots in this way is to some extent arbitrary, but again this was chosen to best represent the experimental electron diffraction patterns. For example, inspection of the experimental electron diffraction patterns in Figs. 4, 9 and 16 shows that reflections for which the angle φ between $[pqr]^*$ and its projected streak direction $[p'q'r']^*$ is 0 to 28° are streaked, whereas those for which φ is 55 or 70·5° are not. The streaking of spots in $\langle 001 \rangle_{Al}$ electron diffraction patterns can be accounted for by both streaking and splitting of spots due to the near-superposition of reflections from Ω precipitates on two different $\{111\}_{Al}$ planes, as the direction of splitting is parallel to the streak direction of the two reflections.

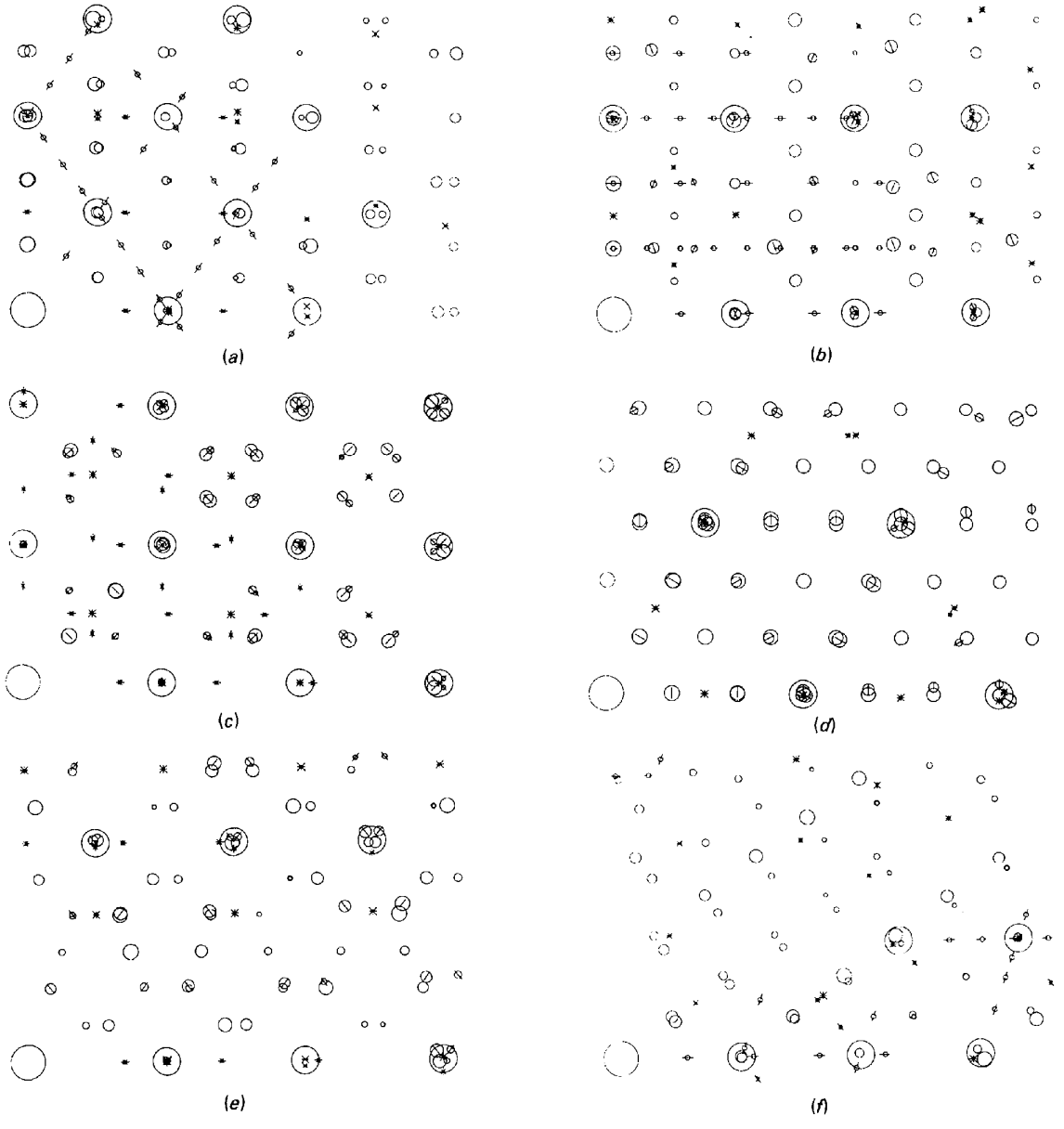

Fig. 18. Quadrants of simulated electron diffraction patterns taking streaking of θ' and Ω precipitate reflections into account. In each case the 000 reflection is at the bottom left. (*a*) $[1\bar{1}0]_{Al}$ for 100 kV electrons, (*b*) $[\bar{2}11]_{Al}$ for 500 kV electrons, (*c*) $[001]_{Al}$ for 500 kV electrons, (*d*) $[111]_{Al}$ for 500 kV electrons, (*e*) $[310]_{Al}$ for 500 kV electrons, (*f*) $[\bar{8}71]$, 6·59° from $[\bar{1}10]$, for 100 kV electrons. Matrix Al reflections are denoted by large circles and θ' reflections are marked with an asterisk to distinguish them from Ω reflections.

Comparison of the data presented in Tables 5–8 and in Fig. 18 with the experimental electron diffraction patterns shows that the simple model in §5 can indeed explain the main features of the electron diffraction patterns once double diffraction is taken into account. The effect of double diffraction is most apparent for the θ' reflections in the $\langle 110\rangle_{Al}$ diffraction patterns (see for example the extra streaks around 000 in Fig. 9), and in the diffraction patterns where the beam direction has been tilted away from $[1\bar{1}0]_{Al}$. For example, when tilting away from the $[\bar{1}10]$ zone, keeping the $g = 111$ systematic in the diffraction pattern, the schematic of a zone such as the $[\bar{6}51]$ zone in Fig. 18 has fewer precipitate diffraction spots around prior $11\bar{1}$ and 002 matrix diffraction positions than the experimental diffraction pattern in Fig. 14(*b*). However, electrons which have been scattered by the θ' precipitates on $\{100\}_{Al}$ and $\{010\}_{Al}$ planes can also be scattered by the matrix Al along 111 and $\bar{1}\bar{1}\bar{1}$ reciprocal-lattice directions, and hence four spots, two due to the θ' precipitates on the $\{100\}$ and $\{010\}$ planes and two due to the Ω precipitates on $\{\bar{1}11\}$ and $\{1\bar{1}1\}$ planes, will be found at prior $11\bar{1}$ and 002 matrix positions forming a characteristic quadrilateral in which the Ω reflections are separated by a reciprocal-lattice vector parallel to the projection of 002_{Al} onto the plane normal to $[\bar{6}51]$. Note that this separation between the two Ω spots increases as the beam direction is rotated away from $[\bar{1}10]$ in such a way that a systematic row of 111 reflections is maintained in the electron diffraction pattern. The second effect of double diffraction is to even out intensities between precipitate reflections separated by reciprocal-lattice distances corresponding to allowed Al matrix g vectors; this is most apparent in the $[\bar{2}11]$ diffraction pattern where 'spots' occur at positions where the orthorhombic F Bravais lattice of the Ω precludes any kinematical reflection.

The degree of fit between experiment and theory is most satisfactory: the theoretical model accounts for the observed splitting of the Ω precipitate reflections at high g along 002 matrix directions in the $\langle 110\rangle_{Al}$ electron diffraction patterns and also accounts for the faint streaking of precipitate reflections at positions such as $\frac{1}{3}(13\bar{1})$ in the $[\bar{2}11]_{Al}$ electron diffraction pattern. It can also account for the very faint reflections seen at positions such as $\frac{1}{2}, \frac{5}{6}, \frac{1}{6}$ and $\frac{1}{2}$, 1, 0 and for the reflections seen at positions such as $\frac{1}{2}, \frac{3}{2}, -\frac{1}{2}$ in the $[\bar{2}11]$ electron diffraction pattern. Faint spots at the centres of the rhombi formed in the $[110]_{Al}$ electron diffraction patterns by the thinness of the Ω precipitates along $\{\bar{1}11\}$ reciprocal-lattice directions can be interpreted as coming from electrons which have been scattered by the ellipsoidal θ' (001) precipitates and then scattered by the Al matrix, and indeed dark-field images from such reflections light up these θ' precipitates strongly with a residual matrix background intensity. However, these θ' precipitates would be expected to contribute to such images anyway because of the streaking along the 001 reciprocal-lattice directions. The alternative explanation is that double diffraction from the matrix and the θ' precipitates inclined at 45° to the electron beam in this orientation causes these faint spots, but no experimental evidence could be found for this.

It is interesting to vary the lattice parameters used to describe the unit-cell dimensions of the Ω precipitates to see the effect this has on the diffraction patterns. If the Ω precipitates are simply considered to have the same lattice parameters as θ (*i.e.* without the orthorhombic distortion), then our calulations suggest that the Ω reflections from a set of three variants on a particular set of $\{111\}$ matrix planes would no longer be coincident, and that therefore there would be further splitting of Ω precipitate reflections in electron diffraction patterns. That such splitting is not observed experimentally suggests that there is indeed an orthorhombic distortion of the tetragonal θ structure in these Ω precipitates. If we then fix the a:b ratio of the dimensions of the orthorhombic unit cell to be $1:\sqrt{3}$ and vary the magnitude of the cell side a, subtle shifts in the positions of the spots and streaks occur which are most noticeable at high g. For example, if $a = a_0\sqrt{3}/\sqrt{2}$, the centres of the Ω reflections near the $\{331\}$ type matrix reflections in a $[\bar{1}10]_{Al}$ electron diffraction pattern are collinear with the matrix spot; this is no longer the case if a is altered, although the splitting of the Ω spots will still be along the 002 matrix reciprocal-lattice direction. Again, comparison of the simulated electron diffraction patterns with the experimental ones suggest that taking the unit-cell edge a to be equal to $a_0\sqrt{3}/\sqrt{2}$ is very reasonable, and we therefore have confidence in the orthorhombic unit-cell dimensions shown in Table 2.

6. HREM image simulations

HREM image simulations were carried out as a function of thickness and defocus to try to understand further the structure of the Ω precipitates. Two simple models were simulated on the basis of the orthorhombic crystal structure and a chemical composition of Al_2Cu given in Table 2, one of the pure Ω structure and the second a model in which a thin Ω precipitate was sandwiched between matrix aluminium. For this latter model, a precipitate thickness parallel to a set of matrix 111 planes of $2c$ was chosen, embedded in the middle of 41 matrix 111 planes to form an orthorhombic supercell of dimensions $a_{ss} = a_0\sqrt{3}/\sqrt{2}$, $b_{ss} = 3a_0/\sqrt{2}$ and $c_{ss} = 2c_\Omega + 41a_0/\sqrt{3}$ which repeated periodically over all space. Matching of the Al and Ω structures was achieved by inspecting corresponding $(111)_{Al}$ and $(001)_\Omega$ atomic projections such as those in Fig. 19, assuming that the structure of the Ω precipitates is that given in Table 2. Clearly, if the precipitate thickness is chosen to be $2c$ with all the

atoms in the unit cell as drawn in Fig. 19 included in the precipitate (*i.e.* from $z = 0$ up to and including $z = 2$), then C stacking planes in the Al can fit well with the precipitate on either side of the precipitate, so that the supercell has a stacking sequence within it of ... $ABC \mid \Omega \mid CABC$ ...

The number of matrix Al planes in the supercell was chosen to generate a structure without any stacking faults at the edges of the supercell, so that B matrix planes were nearest $z = 0$ in the supercell and A matrix planes nearest $z = 1$. In order to keep the model simple, no translational shifts or relaxations in atomic positions were applied in the vicinity of the precipitate–matrix interface. A 1024 × 16 set of Fourier coefficients was generated for the supercell for slice thickness of either 4·96 or 4·30 Å depending on the matrix projection direction of interest, ⟨110⟩ or ⟨211⟩. For the pure Ω structure with a much smaller unit cell, a 64 × 128 set of Fourier coefficients was used, with the same slice thicknesses. Images were simulated in the normal way with a suite of programs developed by Dr G. J. Wood (University of Melbourne), by including the effects of spherical aberration and defocus terms in the objective lens propagator for a 500 kV microscope with $C_s = 2{\cdot}7$ mm and a spread of focus Δ of 150 Å. Results from the simulations are presented in Figs. 20 and 21 for the two models of interest and for each of the four orientations of the precipitate in Figs. 2 and 3. The thickness and defoci in these simulations have been chosen to try and achieve as good a match as possible with the *form* of the experimental images in Figs. 6, 7, 10 and 11 (but not necessarily the exact details of, for example, the precipitate thickness and interfacial ledge structure). Thus, the pseudo-square distribution of either black or white spots and the centred rectangular arrangement of spots in the precipitate images from $\langle 211 \rangle_{Al}$ zones can be simulated, as can the two distinct forms of rectangular and centred rectangular image of the precipitates in the $\langle 110 \rangle_{Al}$ zones. Near Scherzer defocus and for thin specimens, the bright spots correspond to 'holes' in the projected potential of the Ω structure (*cf.* Figs. 2 and 3).

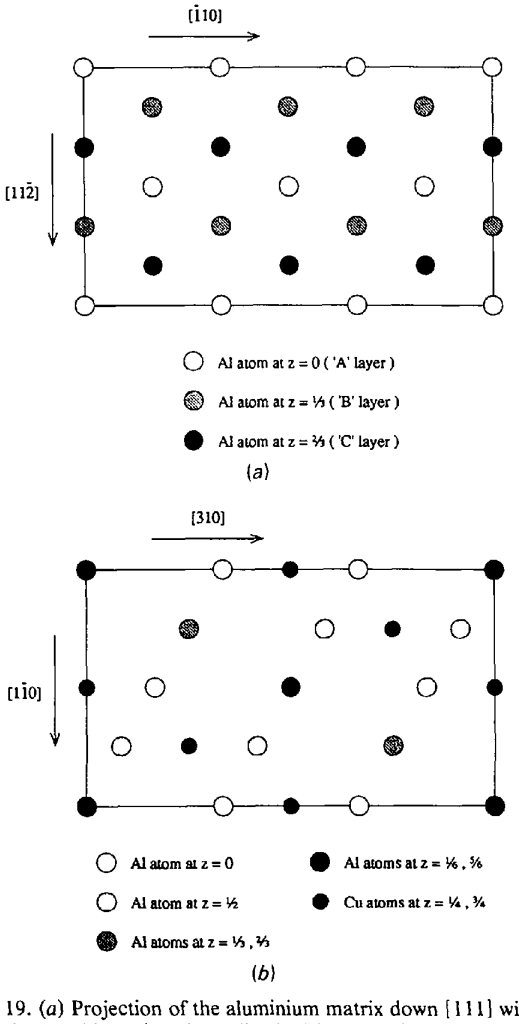

Fig. 19. (*a*) Projection of the aluminium matrix down [111] with an orthorhombic unit cell outlined. (*b*) Projection of the orthorhombic Ω structure down [001].

The good matching obtained lends further support to the orthorhombic unit-cell model for the Ω precipitates, although it should be emphasized that HREM is a relatively insensitive technique for extracting *chemical* information, and so any preferential segregation of Mg and Ag atoms to the Ω precipitates need not be reflected in a recognizable change in the image simulations from the ones shown here. A further point of interest which the simulations bring out well is that the Ω images are affected by the neighbouring Al matrix, and so the change in image as a function of defocus of the Ω precipitate region for a given thickness is different for the two models. This is by no means unexpected – images from thin metallic multilayers and spinodal decomposition materials show similar effects. This also indicates that a much more detailed image analysis would have to be done to characterize fully the precipitate–matrix interfacial structure.

7. Conclusions

A detailed reanalysis of the Ω precipitates in Al–Cu–Mg–Ag alloys has shown unequivocally that the hexagonal structural model proposed by Kerry & Scott (1984) is incorrect and that the structural model proposed by Auld (1986) can indeed account for dark-field transmission electron microscope observations, HREM and the occurrence of extra reflections in electron diffraction patterns from alloys containing these precipitates. Reexamination of Auld's model has shown that the structure he proposes is in fact orthorhombic and is perhaps best regarded as a slightly distorted and presumably chemically modified *coherent* form of θ, albeit a form of θ which is coherent with the

matrix Al in just two dimensions. However, the detailed chemical composition of these precipitates remains unclear, despite good matching of HREM image simulations with experiment for an Ω composition of Al_2Cu.

We would like to thank Professor I. J. Polmear for many helpful discussions during the course of this work. One of us (KMK) would also like to thank the Royal Society for financial support. We are both grateful to Professor D. Hull for the provision of laboratory facilities.

APPENDIX

Diffraction geometry of precipitate shape effects

Ω precipitate reflections will be streaked along $\langle 111\rangle^*_{Al}$ reciprocal-lattice directions because of the thinness of the precipitates in these directions. The projected streak directions for precipitates on each set of $\{111\}_{Al}$ planes are given in Table 4 for the matrix zones $[1\bar{1}0]$, $[\bar{2}11]$ and [001]. The relevant formulae to calculate these projected streak directions are derived by Hirsch, Howie, Nicholson, Pashley & Whelan (1977). These projected streak directions agree with those in the

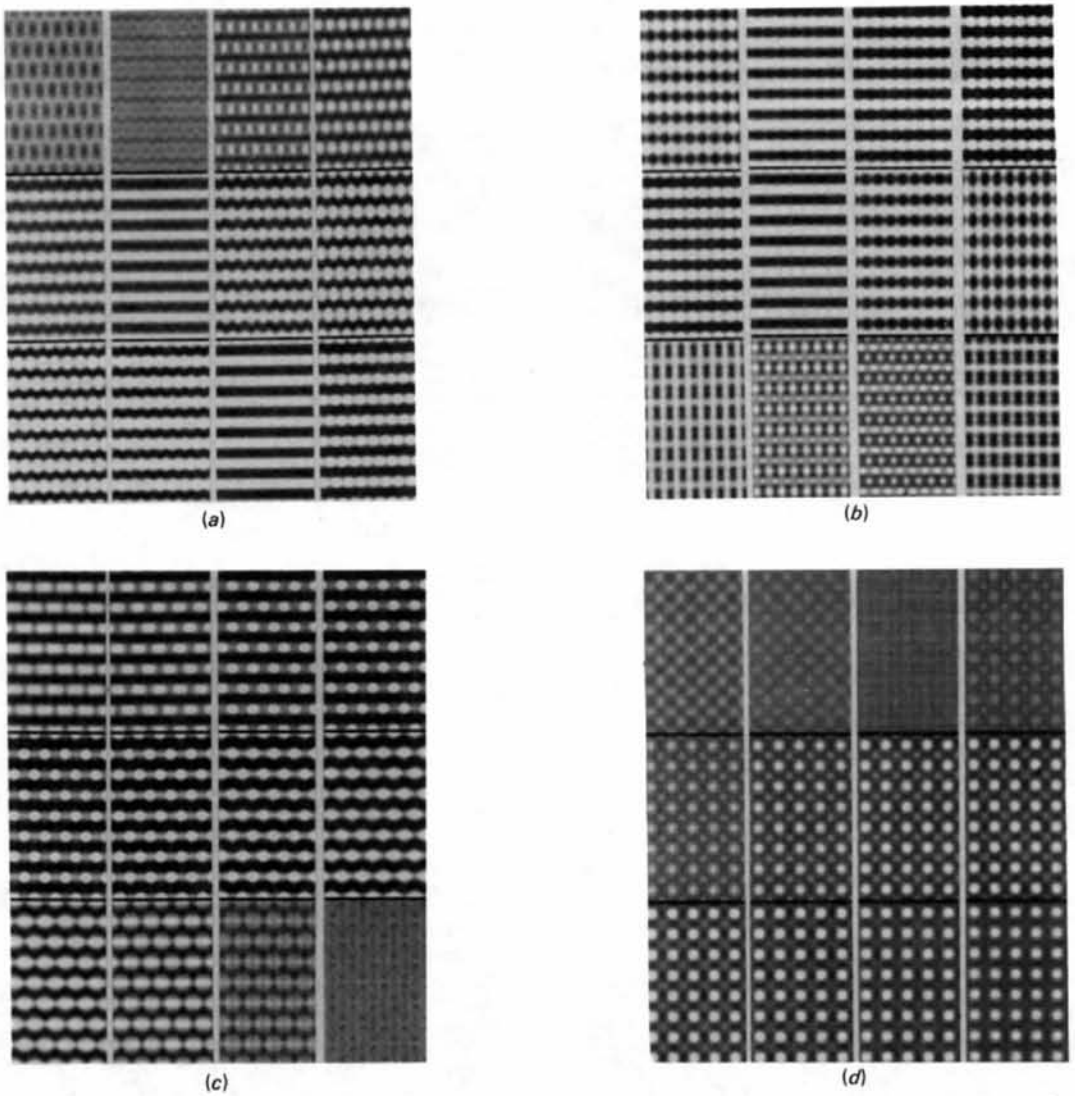

Fig. 20. Image simulations for the model where the Ω structure alone is used. (*a*) Zone axis $[310]_O = [120]_M$, for which the atomic projection of the Ω precipitate is shown in Fig. 2(*a*). 129 Å thick crystal. Defocus values (left to right, top to bottom) are from 0 to −1100 Å in steps of −100 Å. (*b*) Zone axis $[0\bar{1}0]_O = [1\bar{1}0]_M$, for which the atomic projection of the Ω precipitate is shown in Fig. 2(*b*). Defocus and thickness values as in (*a*). (*c*) Zone axis $[1\bar{1}0]_O = [100]_M$, for which the atomic projection of the Ω precipitate is shown in Fig. 3(*a*). 99 Å thick crystal. Defocus values (left to right, top to bottom) are from −100 to −760 Å in steps of −60 Å. (*d*) Zone axis $[100]_O = [110]_M$, for which the atomic projection of the Ω precipitate is shown in Fig. 3(*b*). Thickness and defocus values as in (*c*).

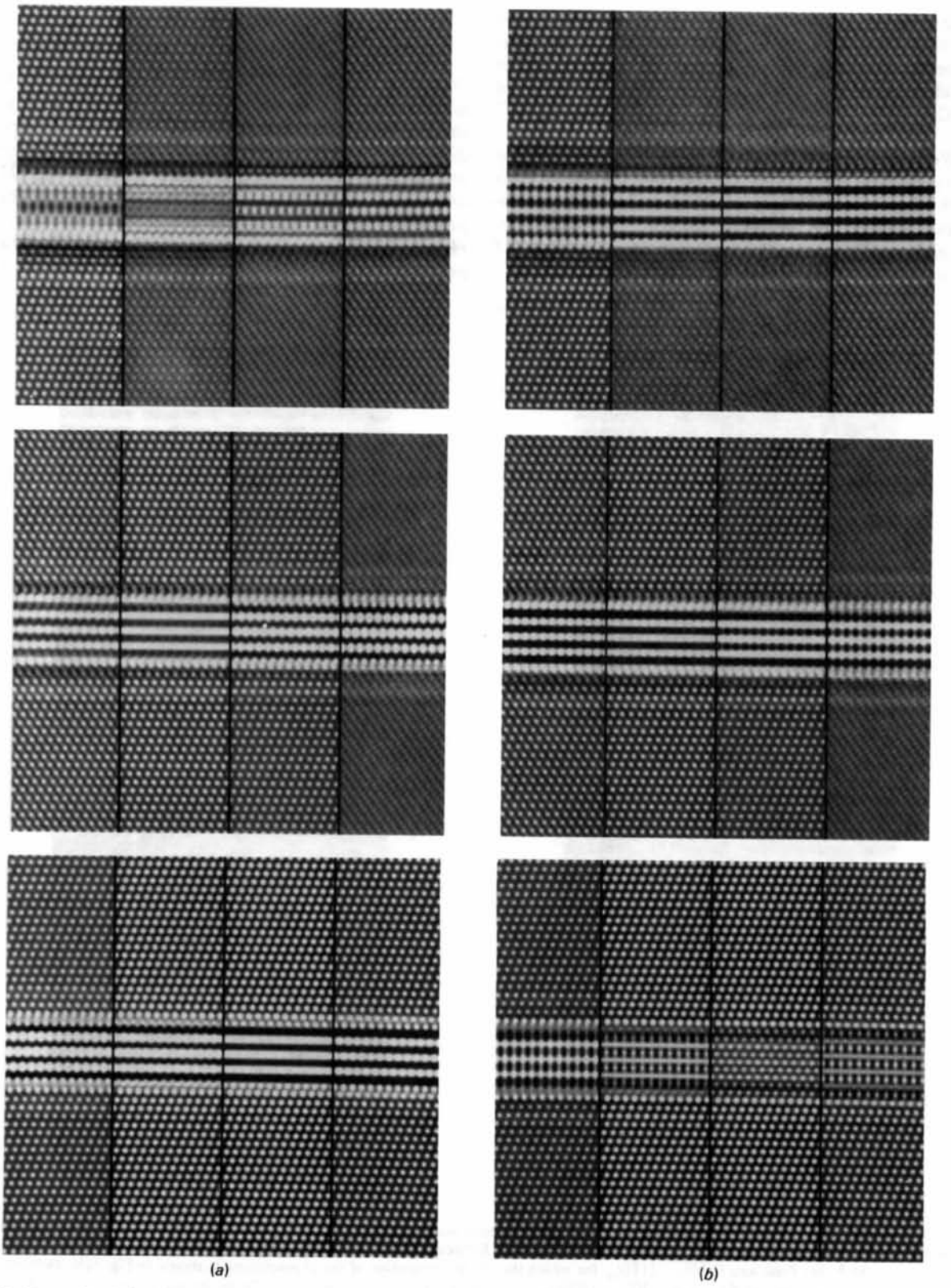

Fig. 21. Image simulations for the supercell model described in the text where a thin Ω precipitate is sandwiched between (111) planes of matrix aluminium. (*a*) As in Fig. 20(*a*), with a $\langle 110 \rangle_{Al}$ zone axis. (*b*) As in Fig. 20(*b*), with a $\langle 110 \rangle_{Al}$ zone axis.

experimental diffraction patterns, and in particular account for the streak directions of the spots at positions such as $\frac{1}{3}, -\frac{1}{3}, 1$ and $\frac{1}{3}, -1, \frac{5}{3}$ in the $[\bar{2}11]$ zone diffraction pattern in Fig. 4.

To account for the *positions* of the extra spots in the diffraction patterns arising from the presence of the Ω precipitates, it is convenient to use a matrix orthonormal coordinate system to define positions. Given the orientation relationships between the precipitates and matrix in Table 3, it is straightforward to calculate the elements of a matrix ${}_MT_P$ relating the components of vectors expressed in the precipitate coordinate system P with the components expressed in the matrix orthonormal coordinate system M through a formula

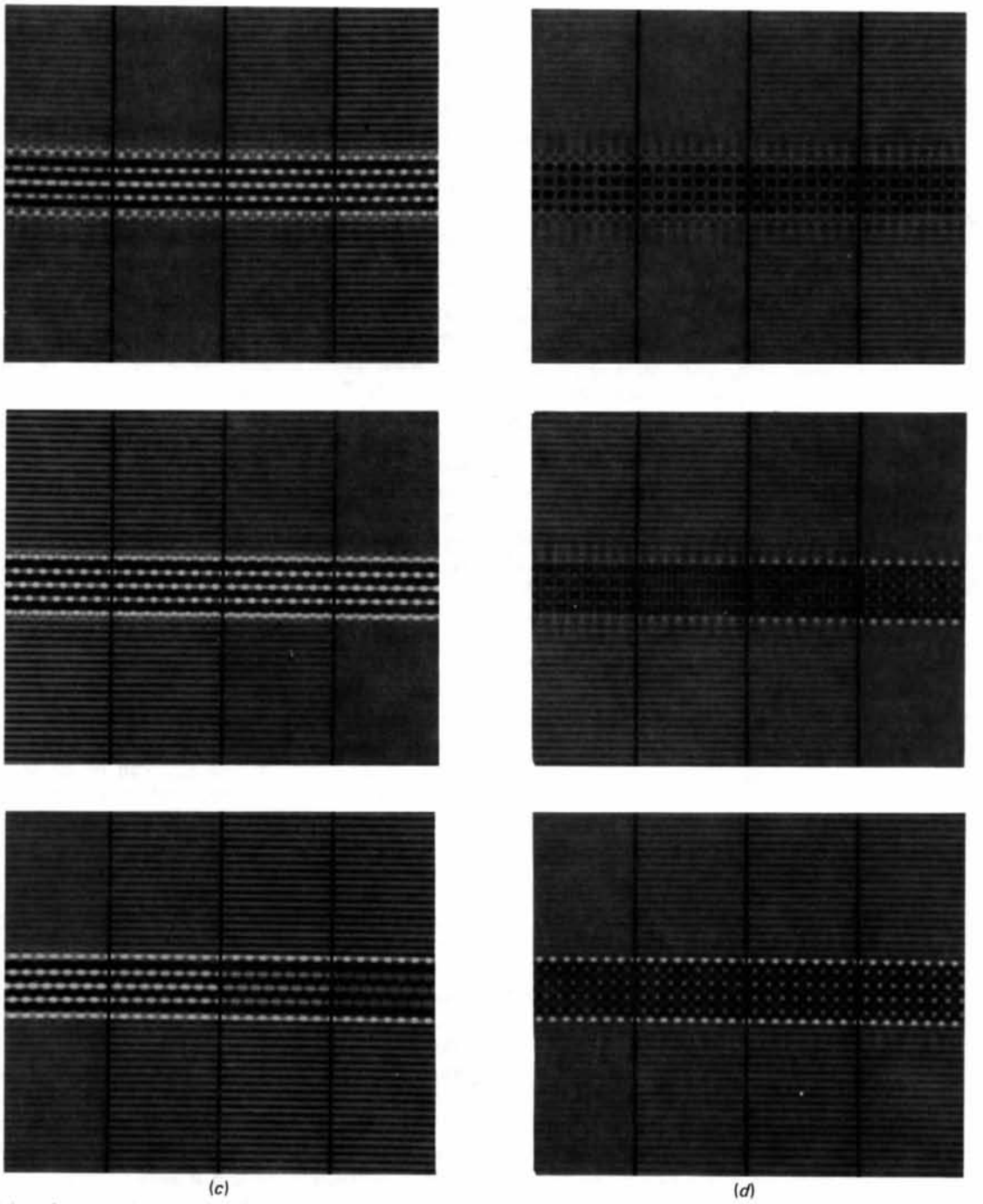

Fig. 21 (cont.). Image simulations for the supercell model described in the text. (*c*) As in Fig. 20(*c*), with a $\langle 211 \rangle_{Al}$ zone axis. (*d*) As in Fig. 20(*d*), with a $\langle 211 \rangle_{Al}$ zone axis.

$$v_M = ({}_M T_P) v_P$$

for each of the 12 variants. Similarly, the components of plane normals are related through the formula

$$\tilde{n}_M = \tilde{n}_P ({}_M T_P)^{-1}$$

where the tilde denotes a transpose operation. Thus, for variant Ω_{11} in Table 3

$${}_M T_P = \begin{bmatrix} 0{\cdot}5 & -1{\cdot}0 & 1{\cdot}209 \\ 0{\cdot}5 & 0{\cdot}5 & 1{\cdot}209 \\ -1{\cdot}0 & 0{\cdot}5 & 1{\cdot}209 \end{bmatrix}$$

if we take the lattice parameter a_0 of aluminium to be 4·96 Å and the lattice parameters a and c of the monoclinic description of the Ω structure to be $a_0\sqrt{3}/\sqrt{2}$ and 8·48 Å respectively, following the data provided by Auld (1986) and Kerry & Scott (1984). On this description, [100] of the monoclinic unit cell of the Ω precipitate is exactly the same length as its corresponding $\frac{1}{2}\langle 112\rangle$ matrix aluminium direction.

For an Ewald sphere of infinite radius (*i.e.* $\lambda = 0$), a precipitate reflection hkl (referred to the matrix coordinate system) streaked along pqr^* (also referred to the matrix coordinate system) will intersect the plane normal to a beam direction $[uvw]$ at a position $h-\xi p$, $k-\xi q$, $l-\xi r$, where

$$\xi = (hu + kv + lw)/(pu + qv + rw). \qquad (1)$$

Assuming the streak is long enough to intersect the Ewald sphere, $h-\xi p$, $k-\xi q$, $l-\xi r$ will be the position of the reflection hkl in the $[uvw]$ diffraction pattern. This result is a good approximation for electrons at 100 and 500 kV, but it cannot account for the separation of spots at high g, as this separation occurs *because* of the finite radius of the Ewald sphere.

For an Ewald sphere of radius $k = |1/\lambda|$, and with reference to Fig. 17,

$$\mathbf{g}.\mathbf{g} = 2\mathbf{k}.\mathbf{g}$$

for reflections lying on the Ewald sphere (Bragg's law). With

$$\mathbf{g} = (h-\xi p, k-\xi q, l-\xi r)$$

and

$$\mathbf{k} = (|\mathbf{k}|/|uvw|)[u\ v\ w]$$

referred to the orthonormal matrix vector basis, Bragg's law becomes

$$(hu+kv+lw) - \xi(pu+qv+lw) = (\lambda/2)(u^2+v^2+w^2)^{1/2}$$
$$\times \{(h^2+k^2+l^2) - 2\xi(hp+kq+lr) + \xi^2(p^2+q^2+r^2)\}, \qquad (2)$$

which is merely a quadratic equation for ξ. If solving this equation gives two real values of ξ, then these two values will define the positions where a chord parallel to $[pqr]^*$ passing through hkl intersects the Ewald sphere. Clearly, only one of the two possible values of ξ will be physically significant in terms of the possible length of a streak. Furthermore, as the wavelength λ tends towards zero, the only solution of ξ obtained is the one derived above for a sphere of infinite radius.

If $[pqr]^*$ and $[hkl]^*$ are both perpendicular to $[uvw]$, a real value of ξ is only obtained when $[pqr]^*$ is parallel to $[hkl]^*$, in which case $\xi = (h^2+k^2+l^2)^{1/2}$, the distance of the reciprocal-lattice spot hkl from the origin. If imaginary values of ξ are obtained, then this corresponds physically to a case where the streak along $[pqr]^*$ will not intersect the Ewald sphere at all, for which P in Fig. 17 has to lie outside the Ewald sphere.

Clearly, therefore, solving (2) for real values of ξ up to a physically significant maximum value ξ_{max} to find those streaked reflections which intersect the Ewald sphere, then computing the position B, where the streak intersects the Ewald sphere, and then computing B', the projection of B onto the plane normal to $[uvw]$, does not account for all of the possible streak geometries. In particular, setting a ξ_{max} will have the effect of eliminating reflections for which the streak intersects the Ewald sphere tangentially at the origin, *i.e.* those for which $[pqr]^*$ is parallel to $[hkl]^*$ and for which $hu + kv + lw = 0$.

Positions of matrix aluminium spots for off-axis diffraction patterns such as those in Fig. 14 can be estimated by assuming that the matrix spots are streaked along the zone direction $[uvw]$, and putting an upper value on the allowed deviation parameter of the spot from the Ewald sphere for physically significant values. In this case, the criterion for an allowed reflection is that

$$s = |g^2/2k - \delta s| < s_{max} \qquad (3)$$

for an upper bound s_{max} on s, where δs is the component of the reciprocal-lattice direction $g = [hkl]^*$ parallel to $[uvw]$. If $hu+kv+lw = 0$, this reduces to a simple $g^2/2k$ criterion, and s_{max} can be set to include only those reflections lying within the specific Laue zone of interest, which for all the cases considered in §6 is the zero-order Laue zone.

With a suitable s_{max}, (3) can also be used to estimate whether precipitate reflections lying just outside the Ewald sphere for which $[pqr]^*$ is almost perpendicular to $[uvw]$ will nevertheless contribute to a particular electron diffraction pattern. Such reflections will either have real solutions of (2) which are higher than the ξ_{max}, or else have imaginary values of ξ. However, these reflections can contribute to an electron diffraction pattern because of the finite three-dimensional intensity distribution in reciprocal space centred at $[hkl]^*$ arising from the three-dimensional shape of the precipitates. Thus, in general, precipitate reflections will occur in an electron diffraction pattern if either (2) is satisfied for $\xi <$ some ξ_{max}, in which case the centre of the streak seen on the electron diffraction pattern can be taken to

be the projected position of where the streak intersects the Ewald sphere, or alternatively if (3) is satisfied for $s <$ some s_{max}, in which case the centre of the streak in the electron diffraction pattern can be taken to be the projected position of $[hkl]^*$.

The values of ξ_{max} and s_{max} chosen for any computations will necessarily depend on both the three-dimensional shape of the precipitates and the effect of any local strains around the precipitates. In order to give a guide to these values the simple kinematical theory of electron diffraction can be used. For a linear dimension of t in real space, the corresponding intensity distribution in k space centred about a reciprocal-lattice point hkl takes the form

$$I(k) = I_0 \sin^2 \pi t k / (\pi k)^2$$

[see, for example, Fig. 4.11 of Hirsch, Howie, Nicholson, Pashley & Whelan (1977)]. The Ω precipitates in the HREM images have thicknesses t of the order of 20 Å or less in the 'c' axis direction and disc widths of the order of 400 Å (*e.g.* Fig. 5). If we take the effective 'width' of the intensity distribution along the 'c' axis in reciprocal space to be α/t for some α, then an upper bound on $|\xi_{max}|$ is simply

$$|\xi_{max}| = a_0 \alpha / (2t\sqrt{3})$$

for $\langle pqr \rangle^* = \langle 111 \rangle^*$, where a_0 is the lattice parameter of aluminium. If $\alpha = 1$, in which case the half-peak intensity would represent approximately the value where the spike seen in reciprocal space would end, and if $t = 20$ Å, $\xi_{max} = 0{\cdot}06$, which cannot account for the almost continuous streaking along $\langle 111 \rangle$ matrix reciprocal-lattice directions. However, this value of ξ_{max} can be increased if there is a substantial precipitate population with thickness of less than 20 Å, or if the value of α is greater than 1. Indeed, in a recent study of streaking in electron diffraction patterns from T_1-containing alloys, Cassada, Shiflet & Starke (1987) took $\alpha = 3$ to interpret the streak lengths they observed. Ω precipitates with thickness of much less than 20 Å may well occur, but it would be difficult experimentally to distinguish these from radiation-damage loops which also form on $\{111\}_{Al}$ planes after exposure to 500 kV electrons. For the computations in §5, we have accordingly used a $|\xi_{max}|$ of 0·15 for the Ω precipitates.

A more sophisticated model could be developed to take account of the way in which the intensity distribution around a reciprocal-lattice point is generated and how it will project onto a particular electron diffraction pattern, but as we demonstrate in §6, this simple theory suffices to explain the main features of the electron diffraction patterns from these Al–Cu–Mg–Ag alloys.

References

AULD, J. H. (1972). *Acta Cryst.* A**28**, S98.

AULD, J. H. (1986). *Mater. Sci. Technol.* **2**, 784–787.

AULD, J. H. & VIETZ, J. T. (1969). *The Mechanism of Phase Transformation in Crystalline Solids*, pp. 77–79. London: The Institute of Metals.

BONNET, R. (1980). *Acta Cryst.* A**36**, 116–122.

BONNET, R. & DURAND, F. (1973). *Proceedings of the Conference on In-situ Composites, Lakeville.* NMAB Publication No. 308, pp. 209–233. Washington: The National Academy of Sciences.

CASSADA, W. A., SHIFLET, G. J. & STARKE, E. A. (1987). *Scr. Metall.* **21**, 387–392.

CHESTER, R. J. & POLMEAR, I. J. (1983). *The Metallurgy of Light Alloys*, pp. 75–81. London: The Institution of Metallurgists.

COUSLAND, S. McK. & TATE, G. R. (1986). *J. Appl. Cryst.* **19**, 174–180.

EIKUM, A. K. & NARAYANAN, G. H. (1986). *Proceedings of the 44th Annual Meeting of the Electron Microscopy Society of America*, edited by G. W. BAILEY, pp. 550–551. San Francisco: San Francisco Press.

GUINIER, A. (1942). *J. Phys. Radium*, **3**, 124–136.

HARDY, H. K. & SILCOCK, J. M. (1955–1956). *J. Inst. Met.* **84**, 423–428.

HIRSCH, P. B., HOWIE, A., NICHOLSON, R. B., PASHLEY, D. W. & WHELAN, M. J. (1977). *Electron Microscopy of Thin Crystals.* New York: Krieger.

HUANG, J. C. & ARDELL, A. J. (1986). *Aluminium–Lithium Alloys III*, edited by C. BAKER, P. J. GREGSON, S. J. HARRIS & C. J. PEEL, pp. 455–470. London: The Institute of Metals.

HUANG, J. C. & ARDELL, A. J. (1987). *Mater. Sci. Technol.* **3**, 176–188.

ILER, A. J. (1969). *Mod. Cast.* **55**, 57–59.

International Tables for X-ray Crystallography. (1952). Vol. 1. Birmingham: Kynoch Press.

KERRY, S. & SCOTT, V. D. (1984). *Met. Sci.* **18**, 289–294.

KNOWLES, K. M. & STOBBS, W. M. (1988). In preparation.

KUBEL, E. J. (1986). *Adv. Mater. Prog.* **130**(6), 43–50.

LAIRD, C. & AARONSON, H. I. (1966). *Acta Metall.* **14**, 171–185.

MEYER, P. & DUBOST, B. (1986). *Aluminium–Lithium Alloys III*, edited by C. BAKER, P. J. GREGSON, S. J. HARRIS & C. J. PEEL, pp. 37–46. London: The Institute of Metals.

NOBLE, B. & THOMPSON, G. E. (1972). *Met. Sci.* **6**, 167–174.

POLMEAR, I. J. (1986). *Aluminium Alloys: Their Physical and Mechanical Properties*, Vol. 1. Proc. Conf. held at Charlottesville, Virginia, USA, 15–20 June 1986, pp. 661–674.

RIOJA, R. J. & LUDWICZAK, E. A. (1986). *Aluminium–Lithium Alloys III*, edited by C. BAKER, P. J. GREGSON, S. J. HARRIS & C. J. PEEL, pp. 471–482. London: The Institute of Metals.

SILCOCK, J. M., HEAL, T. J. & HARDY, H. K. (1953–1954). *J. Inst. Met.* **82**, 239–248.

TAYLOR, J. A., PARKER, B. A. & POLMEAR, I. J. (1978). *Met. Sci.* **12**, 478–482.

VAUGHAN, D. & SILCOCK, J. M. (1967). *Phys. Status Solidi*, **20**, 725–736.

VILLARS, P. & CALVERT, L. D. (1985). *Pearson's Handbook of Crystallographic Data for Intermetallic Phases*, Vols. 1 and 2. Metals Park, Ohio: The American Society for Metals.

WILLIAMS, B. E. (1972). *J. Aust. Inst. Met.* **17**, 171–174.